Università degli Studi di Napoli “Federico II”

Scuola Politecnica e delle Scienze di Base
Area Didattica di Scienze Matematiche Fisiche e Naturali

Dipartimento di Fisica “Ettore Pancini”

Laurea Magistrale in Fisica

Search for a new W’ resonance decaying to a top quark and a bottom quark in proton-proton collisions at 13 TeV with the CMS detector at the LHC

Tesi sperimentale

Relatori:
Dott. Alberto Orso Maria Iorio
Prof. Luca Lista

Candidato:
Rosalba Prattico
Matricola N94/373

A.A. 2017/2018

To Salvatore

Acknowledgements

I would like to express my deep gratitude to Dr. A.O.M. Iorio, supervisor of this work, for his extraordinary professionalism and humanity, which make him, not only a good teacher, but also and above all an example to follow.
My grateful thanks are also extended to my other two supervisors Prof. L. Lista and Prof. F. Tramontano for the great availability and courtesy shown to me, for their advice and for the time they have dedicated to me.
I would like also to thank the CMS Naples group, especially to Agostino, always ready to help despite his numerous commitments, and to Lorenzo, excellent listener and always kind.
Thanks also to "*Istituto Nazionale di Fisica Nucleare*" for giving me the extraordinary opportunity to visit and work at CERN.
A special thanks goes to my family, for supporting me and inciting me to do my best, and to Salvatore, for being exactly as he is.

Contents

Introduction

The Large Hadron Collider (LHC) is the world's largest hadron accelerator designed to provide proton-proton collisions at a design centre of mass energy of $\sqrt{s} = 14$ TeV, and with a design luminosity of $10^{34} cm^{-2} s^{-1}$.
Around the collision points the LHC is equipped with four main experiments (ALICE, ATLAS, CMS and LHCb) in order to provide further proofs on the validity of the Standard Model (SM) of particle physics and to give clues of new physics at the TeV scale.
The SM of particle physics is the theory that currently best explains the fundamental components of matter and their interactions.
Over the years the SM has received several experimental confirmations, such as the discovery of the top quark, the Z and W bosons, the tau neutrino, the Higgs boson, but, despite its extraordinary success, it fails to give an explanation for many other phenomena and, as of today, some notable problems are still unresolved.
Several new physics theories beyond the SM have already been formulated to explain these phenomena, and, among them, some predict the existence of new charged gauge bosons, as W' bosons.
The W' boson is a hypothetical gauge boson that arises from extensions of the electroweak symmetry of the SM, has spin 1 and electric charge ± 1 and it can be detected directly with proton-proton collisions at the LHC in its leptonic dacay channel ($W' \longrightarrow l\nu_l$) or in its hadronic dacay channel ($W' \longrightarrow$ tb), or indirectly through its effects on low-energy processes, such as muon decay where it can replace the W boson of the SM.
The aim of this thesis is to search for a new W' resonance, decaying to a top quark and a bottom quark, using 35.9 fb^{-1} of proton-proton collision data delivered by the LHC at a centre of mass energy of $\sqrt{s} = 13$ TeV and collected by the CMS experiment in 2016. The final state under investigation consists of a top quark that decays hadronically, and a b jet.
This thesis is organized in five chapters:

- **Chapter 1**: description and operation of the LHC accelerator machine and the CMS experiment;
- **Chapter 2**: brief introduction of the Standard Model and description its unsolved issues;

- **Chapter 3**: theoretical and experimental state of the art concerning the W' boson physics;
- **Chapter 4**: signal characterization, final state and description of the algorithms used to identify and reconstruct physical objects of interest for the presented physics analysis;
- **Chapter 5**: analysis strategy with description of the data set and the MC simulation used, of the the event selection, of the background estimation and the fit procedure with its results.

Chapter 1

The LHC accelerator and the CMS experiment

At the end of the Second World War, European science was no longer world-class, in fact in those years the main research centers were located in the USA, so the need was felt to found a European cutting-edge research center. With the task of translating that desire into reality, in 1952 twelve European countries (Belgium, Denmark, France, the Federal Republic of Germany, Greece, Italy, the Netherlands, Norway, Sweden, Switzerland, the United Kingdom and Yugoslavia) assembled a council of scientists that was named, in French, *Conseil Européen pour la Recherche Nucléaire* (European Council for Nuclear Research), with the acronym CERN[1].
On 29 September 1954 the project of the European research center comes to life and the *Organisation Europenne pour la Recherche Nuclaire* (European Organization for Nuclear Research) was born retaining the same acronym as the provisional council after it was dissolved.
The organization is located on the border between Switzerland and France on the north-west outskirts of the city of Geneva and, today, has 22 member states plus some observers, including non-European countries.
CERN is currently the largest research center in high energy physics and provides the necessary tools to explore the intimate nature of matter and the forces that govern it and to study the nature of the universe, its origins and its evolution. Among these instruments there are accelerators, which allow to accelerate at close to the speed of light the constituents of matter and then collide them, and detectors, as they allow to produce and observe particles under controlled conditions.
CERN operates a network of accelerators, built in various periods of CERN history starting from the foundation of the institute. From the beginning, it has been planned that every new and more powerful machine would use the previous ones as "injectors", creating a chain of accelerators that gradually brings a beam of particles to ever higher energies. To allow this chain to

function, all the accelerators are coordinated by a single reference signal, generated by an atomic clocks system and distributed throughout the installation, with an accuracy of the order of the nanosecond.
Currently active machines are:

- two linear accelerators (LINAC 2 and LINAC 3). Linear accelerators use radiofrequency cavities to charge cylindrical conductors. The particles pass through the conductors, which are alternately charged positive or negative. The conductors behind them push and the conductors ahead of them pull, causing the particles to accelerate. Superconducting magnets ensure particles remain in a tight beam.
  LINAC 2 accelerates protons, obtained from hydrogen molecules that pass through an electric field that spill off their electrons, to 50 MeV into the Proton Synchrotron Booster (PSB), while LINAC 3 provides heavy ions, currently lead ions obtained by stripping away the electrons from the molecules, at 4.2 MeV for nucleon into the Low Energy Ion Ring (LEIR).

- Proton Synchrotron Booster (PS Booster), is made up of four superimposed synchrotron rings that receive beams of protons from the linear accelerator Linac 2 at 50 MeV and accelerate them to 1.4 GeV for injection into the Proton Synchrotron (PS).
  Before the Booster received its first beams on 26 May 1972, protons were injected directly from the linac into the PS, where they were accelerated to 25 GeV. The low injection energy of 50 MeV limited the number of protons the PS could accept. The Booster allows the PS to accept over 100 times more protons, which greatly enhances the beam's use for experiments.

- Low Energy Ion Ring (LEIR), accelerate ions from the LINAC 3 to the Proton Synchrotron (PS) to provide ions for collisions within the Large Hadron Collider (LHC). LEIR receives long pulses of lead ions from Linac 3 and transforms them into the short, dense bunches splitting each long pulse into four shorter bunches, each containing 2.2108 lead ions. It takes about 2.5 seconds for LEIR to accelerate the bunches, in groups of two, from 4.2 MeV to 72 MeV. The ions are then at a suitable energy to be passed to the PS.

- Proton Synchrotron (PS), was CERN's first synchrotron, beginning its operation in 1959. With a circumference of 628 metres, the PS has 277 conventional (room-temperature) electromagnets, including 100 dipoles to bend the beams round the ring. The accelerator operates at up to 25 GeV. Currently the PS is a key component in CERN's accelerator complex, where it usually accelerates either protons delivered by the PS Booster or heavy ions from the LEIR.

- Super Proton Synchrotron (SPS), a circular accelerator with a diameter of 2 kilometres built in a tunnel which started in 1976. It was designed to deliver an energy of 300 GeV and was gradually upgraded to 450 GeV, has 1317 conventional (room-temperature) electromagnets, including 744 dipoles to bend the beams round the ring. Besides it being used for fixed-target experiments (currently COMPASS and NA62), it has been operated as a protonantiproton collider (the SppS collider), and for accelerating high energy electrons and positrons which were injected into the Large ElectronPositron Collider (LEP). Since 2008, it has been used to inject protons and heavy ions into the Large Hadron Collider (LHC). It will also soon feed the AWAKE expriment which aims to test new techniques for accelerating particles. Research using SPS beams has probed the inner structure of protons, investigated natures preference for matter over antimatter, looked for matter as it might have been in the first instants of the universe and searched for exotic forms of matter. A major highlight came in 1983 with the Nobel-prize-winning discovery of W and Z particles, with the SPS running as a proton-antiproton collider.

- Large Hadron Collider (LHC)[2], is the largest and most powerful accelerator of particles in the world. It was built by the CERN on the border between France and Switzerland between 1998 and 2008 thanks to the participation of over 10000 scientists and engineers, countless research institutes and universities, with the aim of trying to answer several fundamental questions in the physics of elementary particles, as the origin of mass and the asymmetry between matter and antimatter, to perform precision measurements testing the validity of the Standard Model (MS) and researching new physics.

- On-Line Isotope Mass Separator (ISOLDE) is a facility dedicated to the production of a large variety of radioactive ion beams for many different experiments in the fields of nuclear and atomic physics, solid-state physics and materials science. It permits the study of the vast territory of atomic nuclei, including the most exotic species.
  The high intensity proton beam from the Proton Synchrotron Booster is directed into specially developed thick targets, yielding a large variety of atomic fragments. Different devices are used to ionize, extract and separate nuclei according to their mass, forming a low-energy beam that is delivered to various experimental stations. This beam can be further accelerated, allowing for various studies on nuclear reactions.

- Antiproton Decelerator (AD) is a storage ring that produces low-energy antiprotons for studies of antimatter, and creates antiatoms.
  A proton beam that comes from the PS is fired into a block of metal.

These collisions create a multitude of secondary particles, including lots of antiprotons having too much energy to be useful for making antiatoms. They also have different energies and move randomly in all directions. The job of the AD is to tame these particles and turn them into a useful, low-energy beam that can be used to produce antimatter. The AD is composed of bending and focussing magnets that keep the antiprotons on the same track, while strong electric fields slow them down. The spread in energy of the antiprotons and their deviation from their track is reduced by a technique known as cooling. Antiprotons are subjected to several cycles of cooling and deceleration until they are slowed down to around a tenth of the speed of light. They are then ready to be ejected into the antimatter experiments.

The CERN accelerator complex can be seen in the Figure 1.1.

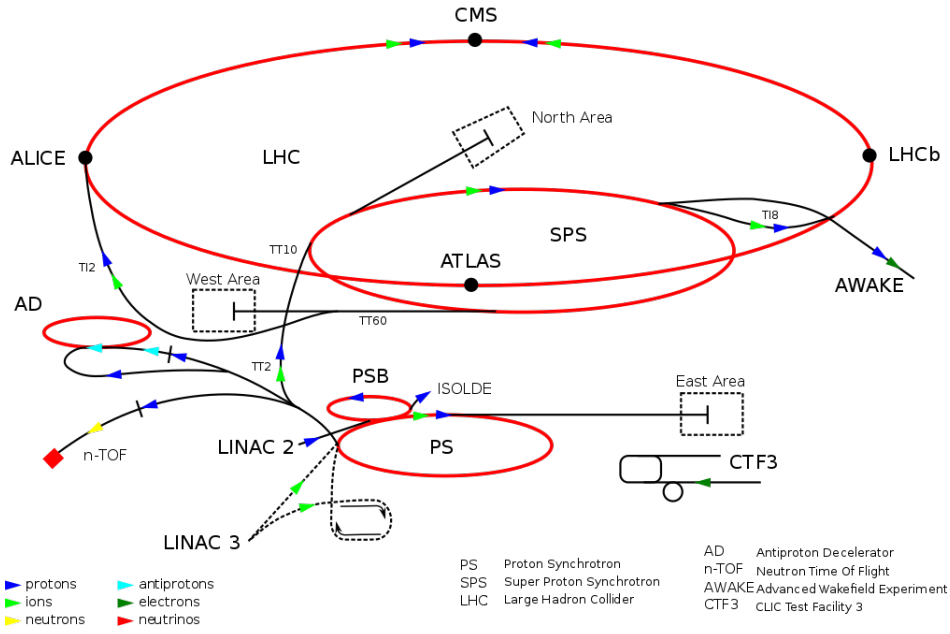

Figure 1.1: The CERN accelerator complex.

Physicists and engineers at CERN are pursuing advanced accelerator research and development for a machine to exploit the Large Hadron Collider's discoveries at the high-energy frontier. The Compact Linear Collider (CLIC) study is an international collaboration working on a concept for a machine to collide electrons and positrons (antielectrons) head-on at energies up to several teraelectronvolts. This energy range is similar to the LHC's, but using electrons and their antiparticles rather than protons, physicists will gain a different perspective on the underlying physics.

1.1 LHC

The LHC is a circular accelerator of hadrons, i.e. protons and heavy ions. The task of this accelerator is to bring the hadrons at close to the speed of light, reaching a set energy, and then collide them in four interaction points where the detectors are located.
The energy range that can be reached spans from 450 GeV per beam, i.e. the injection energy of SPS, up to a maximum of 7 TeV per beam according to the machine's original design specifics, resulting in a centre of mass energy reaching up to 14 TeV .
The machine started a first run of data taking (*Run 1*) in 2010 with a centre of mass energy of 7 TeV, up to 8 Tev in 2012.
After the end of Run 1, in 2013, the LHC has stopped for technical break (detector upgrade and maintenance operations) for two years.
It restarted in 2015 reaching a centre of mass energy of 13 TeV and stopped the data taking in 2018 with a luminosity of $2 \cdot 10^{34} cm^{-2} s^{-1}$.
The 2015-2018 data taking period is called *Run 2*.
The LHC is built inside a 27 km long underground tunnel, at 100 m depth on average, located on the border between France and Switzerland, in a region between the Geneva airport and the Jura mountains, originally excavated to realize the Large Electron-Positron Collider (LEP).
The LHC consists of 1232 dipole magnets 15 metres in length that have the task of keeping the orbit of the beam circular, 392 quadrupole magnets, each 57 metres long, that collimate the beam, from different radiofrequency cavities that accelerate the beam and from hexapolar, ocular and superior magnets that further correct the orbit of the particles.
The magnets are superconductors based on the niobium-titaniun (NbTi) Rutherford cables technology, which need temperatures of the order of 1.9 K to work. This allows circulating currents of the order of 35 kA, capable of producing magnetic fields of 8.3 T.
The entire circuit is cooled by the most impressive refrigeration system in the world with its 96 tons of superfluid helium 4.
Because the space in the tunnel is limited, a twin-bore design is used, in such a way that it is possible to use only one cryogenic structure with proton rings in the same cryostat, but this requires the presence of oppositely oriented magnetic fields to allow the coexistence of two proton beams along the same circumference.
The two beams are kept on parallel orbits and are brought together in a single beam pipe only near the interaction point.
LHC also requires vacuum systems for the insulation of the cryomagnets, for the helium distribution and a beam vacuum. The typical vacua at cryogenic temperatures in the interaction point require a pressure around in the range $10^{-10} - 10^{-11}$ mbar.
The particles that are mainly used in this accelerator are protons coming

from hydrogen gas, produced by using an electric field that deprives the hydrogen atoms of their electrons.
The proton beams, before being introduced into the LHC, pass through a complex of accelerators that increase the energy of the beam up to 450 GeV. The first accelerator is LINAC2 that generates protons of 50 MeV which are placed in PSB that brings the energy of the beam to 1.4 GeV and then send them into the PS that increases the energy up to 25 GeV; then we pass to SPS which carries the protons to 450 GeV which are, finally, placed both clockwise and anticlockwise direction in the main ring. This last, during a session of about 20 minutes, brings the particles to reach the regime energy. The protons are injected into the LHC as bunches of $1.15 \cdot 10^{11}$ protons. Each beam has 2808 circulating proton bunches, which are arranged in groups of 3 and 4 trains of 72 bunches, with 25 ns spacing within the train corresponding to 8 empty bunches between two trains. At every bunch crossing occour the collisions between the beams so the resulting maximum collisions rate is 40 MHz.

An important parameter in an accelerator is the *luminosity*.
The *instantaneous luminosity* $\mathcal{L}(t)$ is the proportionality factor between the cross section of a process σ and the number of events observed per unit of time in the collision R (rate),

$$R = \mathcal{L} \cdot \sigma$$

so it has the dimensions of a flow.
It is also possible to define the *integrated luminosity* L as the temporal integral of instantaneous luminosity,

$$L = \int \mathcal{L} dt$$

The instantaneous luminosity can be measured by the machine parameters taking into account the geometric and kinematic characteristics of the beam. Assuming a Gaussian profile of the beams and a head-on collision, the instantaneous luminosity is given by

$$\mathcal{L} = \frac{N_p^2 n_b f \gamma}{4\pi \epsilon_n \beta^*} F$$

where:

- N_p is the number of particles per bunch;
- n_b is the number of bunches per beam;
- f is the revolution frequency;

- γ is the relativistic Lorentz factor $(1 - v^2/c^2)^{-1/2}$;
- ϵ_n is the normalized transverse beam emittance;
- β^* is the beta function at the collision point and it is a measure of how narrow the beam is at the interaction point;
- F the geometric luminosity reduction factor due to the crossing angle at the interaction point.

The geometric luminosity reduction factor can be written as

$$F = \left(1 + \left(\frac{\theta_c \, \sigma_z}{2\sigma^*}\right)^2\right)^{1/2}$$

with θ_c the full crossing angle of the beams at the interaction point, σ_z bunch length and σ^* transverse RMS beam size at the interaction point. The Table 1.1 shows the values of the parameters above for the operating period of 2016.

Parameter	Value
N_p	$1.6 \cdot 10^{11}$
n_b	2200
f	40 MHz
γ	4260
ϵ_n	2.5 μm
β^*	$0.6m$
θ_c	290 μrad
σ_z	9.4 cm
σ^*	19 μm

Table 1.1: Values of the LHC machine parameters for the operating period of 2016.

The beams with protons rotate for many hours in the LHC beam pipes before colliding in the four points where there are the four main experiments:

- **ALICE** (A Large Ion Collider Experiment) is dedicated to the study of collisions of heavy nuclei (especially Pb-Pb) in a range of very high density in which it is expected to observe the existence of the quark and gluon plasma (QGP), a new state of matter in which, under the conditions of high density and temperature, quarks and gluons are not anymore confined in hadrons.

- **ATLAS** (A Toroidal LHC ApparatuS) and **CMS** (Compact Muons Solenoid) are general purpose dectors, i.e. detectors designed to identify a large variety of experimental signatures in order to allow a wide-ranging study of LHC processes. Among the objectives of the experiments are the study of the top and beauty quarks and the Higgs boson, the search for supersymmetric particles or other particles beyond those provided by the MS.
  The two experiments differ mainly in the configuration of the magnets for the muon detection system, in the first one is toroidal, in the second solenoid, thus affecting also the magnetic field dictating the trajectory of muons and reflecting upon reconstruction techniques.

- **LHCb** (Large Hadron Collider beauty experiment) has been designed and optimized to study the properties of quark b and material-antimatter asymmetry.
  Of the four experiments LHCb is the only one in which the two beams that collide do not have the same energy, in fact one is at regime energy (7 Tev), the other is a injection energy (450 GeV).

1.2 CMS experiment

The CMS detector[3] is built around a huge solenoid magnet, from which it takes its name. This takes the form of a cylindrical coil of superconducting cable that generates a field of 3.8 T, about 100000 times the magnetic field of the Earth. The field is confined by a steel yoke that forms the bulk of the detectors 14000 tons weight.
Instead of being built in-situ like the other giant detectors of the LHC experiments, the CMS detector was constructed in fifteen sections at ground level before being lowered into an underground cavern near Cessy, in France, and reassembled.
The complete detector is 21 metres long, 15 metres wide and 15 metres high. The structure of the CMS is such as to reveal particles deriving from the collision of hadrons and to measure masses, momenta, energies and charges; in fact, the detector consists of several sub-detectors that allow to identify different particles and reconstruct their characteristics with an high momentum resolution on a wide energy and angular coverage.
Working at high luminosities, the detector has been designed to operate in a high radiation environment, maintaining good performances over the course of several years of data taking, and to be able to distinguish processes of interest from backgrounds.
Furthermore it is required that the detector has high granularity, or high spatial resolution, in order to limit the so-called pile up, meaning the overlap between different particles of the same event or coming from interactions in the same bunch-crossing.

The same problem can be had if the detector's response (or the readout electronics) is slower than the nominal time interval between two bunch-crossings, so good time resolution is required.
One of the most important requirements of a detector like CMS is the tightness, for this reason CMS has a cylindrical structure (barrel) that covers the central region, and two caps (endcaps) covering the regions closest to the beams, in order to respect the cylindrical symmetry around the beam axis.
The coordinate system of CMS is a right-handed Cartesian frame centred at the nominal interaction point and oriented in the following way:

- the x-axis points towards the center of the LHC ring and represents the horizontal coordinate;
- the y-axis points upwards, perpendicular to the LHC plane, and represents the vertical coordinate.

  The x-y plane represents the transverse plane respect to the collision axis.
- the z-axis is directed along the anticlockwise direction of the beam and represents the longitudinal direction.

Given the geometry of the CMS (cylindrical symmetry), the coordinate system often used to reconstruct the tracks of particles is a cylindrical coordinate system:

- the radial distance r from the z-axis;
- the azimuth angle ϕ is the angle of rotation around the z-axis with origin identified on the x-axis and increasing clockwise looking in the positive direction of the z-axis;
- the polar angle θ is defined as the rotation angle around the x-axis with origin on the z-axis and increasing clockwise looking in the positive direction of the x-axis.
  A variable often used in place of θ is the *pseudorapidity* η defined as $\eta = -ln[tg(\theta/2)]$. This variable has the advantage that, in relativistic approximation, does transform linearly under boosts along the z-axis, thus resulting in invariant distances between relativistic particles along the z-axis.
  Obviously, as the angle increases from zero, the pseudorapidity decreases from infinity.

Using these coordinates, the distance between two particles directions can be written as another Lorentz invariant variable:

$$\Delta R = \sqrt{(\Delta\phi)^2 + (\Delta\eta)^2}. \tag{1.1}$$

Usually two important variables, referred to the Cartesian system, are the transverse momentum p_T and the transverse energy E_T, defined as:

$$\vec{p_T} = \sqrt{p_x^2 + p_y^2} \tag{1.2}$$

$$E_T = Esin\theta \tag{1.3}$$

1.2.1 The CMS sub-detectors system

Starting from the interaction point and proceeding towards the outside, as shown in Figure1.2, the CMS sub-detectors layout is the following:

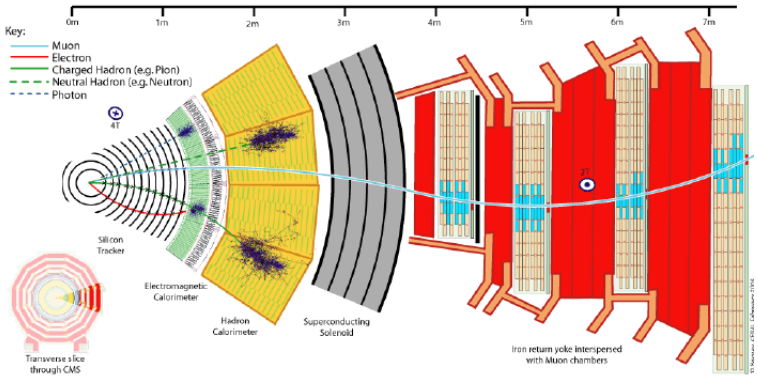

Figure 1.2: The CMS sub-detectors system.

- **tracking system**[4, 5], it accurately measures the positions of passing charged particles allowing to reconstruct their tracks. Charged particles follow spiralling paths in the CMS magnetic field and the curvature of their paths allows to measure their momenta. It has a radius of 1.2 m and a length of 5.8 m and its acceptance is of $|\eta| < 2.5$. It is composed by a high resolution silicon pixel vertex detector and a silicon strip tracker with an active area of 200 m^2:

  - the pixel vertex detector, more internal, fundamental for the reconstruction of particles with a very short average life, contains 65 million pixels and allows to measure the position with an accuracy of 10 μm for the radial measurements and of 20 μm for the transverse measurements.
    This detector consists of cylindrical layers placed at 4 cm, 7 cm and 11 cm from the vacuum tube of the beam, and two discs at each end. Being so close to the collision, the number of particles passing through is huge (the rate of particles received 8 cm from the beam line will be around 10 million particles per cm^2/s), so the pixel detector has to disentangle and reconstruct all the

tracks they leave behind, and withstand such a pummeling over the ten-year duration of the experiment.
Because there are 65 million channels, the pixels are mounted on cooling tubes not to overheat the detector.

– the silicon strip tracker, more external, has a resolution between 35-52 μm in the radial direction and 530 μm in the transverse direction.
The silicon detectors work in much the same way as the pixels: as a charged particle crosses the material it knocks electron from atoms and within the applied electric field these move giving a very small pulse of current lasting a few nanoseconds. This small amount of charge is then amplified by APV25 chips, giving us hits when a particle passes, allowing us to reconstruct its path.
Due to the nature of their job, the tracker and its electronics are pummeled by radiation but they are designed to withstand it. To minimise disorder in the silicon and avoid it causing damage, this part of the detector is kept at -20 C.

Both detectors are present both in the barrel and in the endcaps.
The barrel has three pixel and ten strip layers, while the endcap sections have two pixel and twelve strip layers.
The barrel strips and pixels are parallel to the beam axis, while the endcap ones are disposed orthogonally to it to allow measurement of tracks at higher η.

- **Electromagnetic calorimeter or ECAL**[6], is a hermetic homogeneous calorimeter, with 1.2 m < r < 1.8 m, that measures the energy released by electrons and photons emerging from collisions. They are of particular interest because useful for finding the Higgs boson and other new forms of physics. To find them with the necessary precision in the very strict conditions of the LHC (a high magnetic field, high levels of radiation and only 25 ns between collisions) it was decided to use 61200 lead tungstate ($PbWO_4$) crystals mounted in the central barrel part and 7342 crystals in each of the two endcaps.
The characteristics of the $PbWO_4$ transparent and scintilating crystals (the high density ($8.28 g/cm^3$), short radiation length (0.89 cm) and small Molere radius (2.2 cm)) lead to a fine granularity and a compact calorimeter that succeeds in absorbing electrons and photons in 23 cm of length.
The scintilating material covers a pseudorapidity $|\eta| < 3.0$ and has a decay time of about 10 ns which allows to collect 85% of light in 25 ns.

- **Hadronic calorimeter or HCAL**[7], is a hermetic sampling calorimeter that measures energy released, position and arrival time of hadrons,

such as protons, neutrons, pions, and kaons, and provides indirect measurement of non-interacting, uncharged particles, such as neutrinos, measuring the missing transverse energy.
To reduce the effects of inefficiency and not to have areas where a particle can go unnoticed, HCAL uses alternating layers of absorber made from a non-magnetic material and fluorescent scintillator materials that produce a rapid light pulse when the particle passes through. Special optic fibres collect up this light and feed it into readout boxes where photodetectors amplify the signal.
In order to contain and measure the showers of particles produced by the interaction of a hadron with the absorber material, the minimum thickness of material required is about one meter. To achieve the result, HCAL is divided into barrel (HB and HO), endcap (HE) and forward (HF) sections.
The barrel and endcap sections are located around the ECAL respecting the concentric cylindrical geometry and cover a pseudorapidity range of $|\eta| < 3.0$. They are composed by brass absorber plates interleaved with scintillator tiles embedded with wavelenght shifting (WLS) fibers.
The brass absorber is commonly known as cartridge brass (C26000) and is composed of 70% Cu and 30% Zn, its density is 8.83 g/cm^3 with radiation lenght of 1.49 cm and nuclear interaction length of 16.42 cm.
Into barrel, HB is the last detector placed inside the superconducting coil of the magnet (1.8 m < r < 2.9 m), while HO is placed outside the coil, and ensures that there are no losses of energy from the back of the HB.
Lastly, the HF is located 11.2 m away from the interaction point, allowing to include the pseudorapidity range $|\eta| < 5.0$, and picks up the particles coming out of the collision region at shallow angles relative to the beam line. This receives the bulk of the particle energy contained in the collision so must be very resistant to radiation and use different materials to the other parts of the HCAL, in fact it is made up of quartz fibres embedded within steel absorber and uses a Cherenkov-based technology.

The energy resolution of a calorimeter can be parametrized as:

$$\left(\frac{\sigma}{E}\right)^2 = \left(\frac{a}{\sqrt{E(GeV)}}\right)^2 + \left(\frac{b}{E(GeV)}\right)^2 + (c)^2$$

with:

- a stochastic term, dominant at low energies, takes into account intrinsic statistical shower flutuations, sampling fluctuations and signal quantum fluctuations;

- b noise term, negligible at low luminosity, takes into account both apparent energy due to electronic noise, radio-activity and pileup;
- c constant term, dominant at high energies, takes into account fluctuations of longitudinal leakage, inhomogeneities (hardware or calibration), imperfections in calorimeter construction (dimensional variations, etc.), fluctuation of the electromagnetic component in hadronic shower, non-linearity of readout electronics and fluctuations in energy lost in dead material before or within the calorimeter.

The energy resolution of the electromagnetic calorimeter of CMS is

$$\left(\frac{\sigma}{E}\right)^2 = \left(\frac{2.80\%}{\sqrt{E(GeV)}}\right)^2 + \left(\frac{0.12}{E(GeV)}\right)^2 + (0.30\%)^2$$

while the energy resolution of the hadronic calorimeter of CMS is

$$\left(\frac{\sigma}{E}\right)^2 = \left(\frac{84.70\%}{\sqrt{E(GeV)}}\right)^2 + (7.40\%)^2$$

- The **magnet** used in CMS is composed of a superconducting coil that produce an almost uniform magnetic field, and is built to reach a magnetic field of 3.8 T when electricity flows through it.
  The magnet is the instrument around which the whole experiment is designed and its task is to curve the path of the particles obtained in the collisions of the LHC beams. Once the trajectory is known, it is possible to measure the impulse of a particle and its electric charge.
  To prevent board effects and make that the lines of force of the external magnetic field are as uniform as possible, outside the coil, so as to surround it, there is an iron yoke, composed of alternating layers interspersed with the muon detectors, that allows for a 1.8 T constant field also in the region outside the magnet.
  The magnet has 2.9 m < r < 3.8 m and $|\eta| < 1.4$.

- **Muon system**[8], is a system of muon detectors used for muon identification, momentum measurement and triggering.
  Because the muons can penetrate several meters of iron and of matter in the tracker and in the calorimeters without decay, they have a clean signature, can appear in final states of many new physics processes and can be reconstructed with high precision using information inside and outside the magnet. Their properties make them good candidates for precision measurements.
  CMS uses three different types of gas detectors: Drift Tubes, Resistive Plate Chambers and Cathode Strip Chambers.

The Drift Tubes (DTs), positioned in the barrel. It was possibile to use a drift chamber as the tracking detector for the barrel muon system because of the low expected rate and the relatively low intensity of the local magnetic field.
The CMS barrel muon detector is made of four stations: the first three innermost have 60 drift chambers each, the outermost has 70.
Since at momenta larger than 40 GeV the rate of background generated by neutrons and gammas is from 10 to 100 times larger than the one from prompt muons, a redundancy of information is required and it is obtained by having several layers of separated drift cells per station.
The tracking and timing performance of a chamber was optimized using twelve layers of drift tubes divided into three groups of four consecutive layers, named Super Layers (SL).
Into first three stations, each chamber has the middle SL that measures the coordinate along the direction parallel to the beam (z) and the two outside SLs that measure the perpendicular coordinate (r,ϕ). The fourth station does not contain the z-measuring planes.
To have the global resolution in (r,ϕ) per chamber of 100 μm, the single wire resolution can be better than 250 μm.
The baseline cell has a pitch of 40 mm by 13 mm. At the center is the anode wire, made out of 50 μm diameter stainless steel type 304L. The cathodes defining the cell width are aluminum I-beams 1.2 mm thick and 9.6 mm high. A plastic profile, made of 0.5 mm thick extruded poly-carbonate plastic (Lexan), is glued to the upper and lower parts of the I-beams in order to electrically insulate the cathodes from the aluminum plates.
Each cell of each chamber is offsetted by a half-cell width with respect to their neighbour to eliminate dead spots in the efficiency.
The choice of a tube as the basic drift unit was made in order to obtain protection against the damage from a broken wire and to partially decouple contiguous cells from the electromagnetic debris accompanying the muon itself.

The Chatode Strip Chambers (CSCs), located in the endcaps, are able to provide precise space and time information in the presence of uneven magnetic field and high particle rate thanks to their fast response time, fine segmentation, and radiation resistance.
SCs are multiwire proportional chambers with segmented cathode readout and consist of arrays of positively-charged anode wires crossed with negatively-charged copper cathode strips within a gas volume.
There are four stations of CSCs in each endcap, with chambers having trapezoidal shape and arranged, perpendicular to the beam line, in a

series of concentric rings centered on the beam line.
The stations are separated by the iron disks of the flux return yoke, which are thick enough to isolate the electrons in showers. The last station is followed by a 100 mm thick iron disk whose primary purpose is shielding the station from backsplash backgrounds induced by particles scattered at small angle and interacting with the forward calorimeter, quadrupoles, beam pipe etc.
Each CSC has six layers of wires sandwiched between cathode panels provide robust pattern recognition for rejection of non-muon backgrounds and efficient matching of external muon tracks to internal track segments.
Therefore, each chamber provides six measurements of the ϕ-coordinate (strips) and six measurements of the r-coordinate (wires).
Strip width varies from 3 to 16 mm for different chambers, or from about 2 to 5 mrad in ϕ-coordinates.
Muon identification is ensured over the range corresponding to 10 $< \theta <$ 170.

The Resistive Plates Chambers (RPCs), positioned both in the barrel that in the endcaps, are gaseous parallel-plate chambers that combine a reasonable level of spatial resolution with excellent time resolution, comparable to that of scintillators, and operate in avalanche mode to ensure good operation at high rates.
A resistive plate chamber is constructed of two parallel plates of material made of phenolic resin, with good surface flatness and a high bulk resistivity. Typically the plate separation is on the order of a few millimeters. The resin material is coated with a conductive graphite paint to form electrodes, and readout is made by means of aluminum strips outside the resin plates, insulated from the electrodes by some plastic material.
In the barrel muon system there are six layers of RPCs, two in each of the first two stations, and one in each of the last two stations. In this way it is possible to use the trigger algorithm to work even for low-p_T tracks that may stop before reaching the outer two stations.
In the endcap region, there is a plane of RPCs in each of the four stations in order for the trigger to use the coincidences between stations to reduce background, to improve the time resolution for bunch crossing identification, and to achieve a good p_T resolution.
Finally, a sophisticated alignment system measures the positions of the muon detectors with respect to each other and to the inner tracker, in order to optimize the muon momentum resolution.

These are chosen because the volume to be occupied is very large and they are less expensive than other tracking technologies, besides

they are reliable and robust to the radiation.
The system covers a pseudorapidity range of $|\eta| < 2.4$ and has 4.0 m $<$ r $<$ 7.4 m.

- **Trigger and data acquisition (DAQ) system**, serves to select and store events of potential interest for the analysis.
  At full LHC luminosity, twenty inelastic proton-proton collisions occur every 25 ns, but only a small fraction of them are hard scattering interactions containing events with an interesting signature, and the rest are mostly minimum bias (MB) events.
  Given the high interaction rates, of about 40 MHz, it is impossible to store and process all produced data with the current technologies, so a drastic rate reduction is achieved to allow the writing on mass memory that occurs with a frequency of 100 Hz.
  At CMS, the rate is reduced by the trigger system in two steps called Level-1 (L1) Trigger[9] and High-Level Trigger (HLT)[10], respectively. L1 is an extremely fast (its decision has to be made every 25 ns, without deadtime) and wholly automatic process that looks for simple signs of interesting physics, for instance particles with a large amount of energy, and reduces the event rate from 40 MHz to 100 kHz (50 kHz at low luminosity) making a decision based on the kinematics of the individual object. The triggered objects are then passed to the subsequent DAQ system and HLT for further reconstruction and selection. HLT reduce the rate to 100 Hz, performing more detailed reconstruction of objects: the system assimilates and synchronises the information from different parts of the detector to recreate the entire event and sends it to a farm of more than 1000 standard computers; here the PCs run very complex physics tests to look for specific signatures, for instance matching tracks to hits in the muon chambers, or spotting photons through their high energy but lack of charge.
  The Figure1.3 shows the data flow in the trigger and DAQ system.

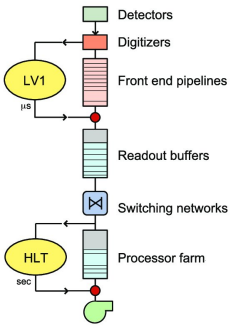

Figure 1.3: Data flow in the trigger and DAQ system.

Chapter 2

The Standard Model of particle physics

Since 1930s, the study and work of thousands of physicists have led to a remarkable understanding of the fundamental structure of matter: the universe is composed from a precise set of basic components, called fundamental particles, and is governed by four fundamental interactions, namely the electromagnetic, the weak, the strong and the gravitational.
The Standard Model (SM) of particle physics is our best understanding of how these particles and three of the forces are related to each other, in particular the electromagnetic and weak interactions, unified in the electroweak force, and the strong interaction. It is a quantum field theory based on a gauge principle for non-abelian transformations, in a way so to be renormalizable and consistent with special relativity.
The term "Standard Model" was first coined by A. Pais and S. Treiman in 1975, but the current form of this model has been the result of years of theories: in 1961 S. Glashow[11] discovered a way to combine the electromagnetic and weak interactions; in 1967 S. Weinberg[12] and A. Salam[13] incorporated the Higgs mechanism[14, 15, 16] into Glashow's electroweak interaction; during the 60s and 70s the theory of the strong interaction, i.e. quantum chromodynamics, was developed by M. Gell-Mann and G. Zweig[17], who suggested the existence of quarks with different flavours, and M.Y. Han with Y. Nambu[18] and O.W. Greenberg[19], who suggested the existence of a new quantum number called *color*; in 1973, D. Politzer[20], D. Gross and F. Wilczek[21] suggested the theory of the asymptotic freedom of strong interaction.
Over the years the SM has received several experimental confirmations, such as the discovery of the top quark, the Z and W bosons, the tau neutrino and the Higgs boson, however, since it does not include the gravitational force, for which there is no consistent quantum theory to date, it does not represent a complete theory of fundamental interactions.

2.1 Fundamental particles

The particles included in the SM are divided into fermions and bosons: the first have semi-integer spin and obey the Fermi-Dirac statistics and the Pauli exclusion principle, while the latter have integer spin and obey the Bose-Einstein statistics.
Fermions are categorized as either quarks or leptons, which are grouped in three generations each. A generation (or family) is a doublet of particles associated to an isospin quantum number. All quark generations contain a particle with +2/3 charge and a particle with charge -1/3, while lepton generations include a particle with charge -1 and a neutral particle, named neutrino.
The leptons interact through electromagnetic and weak interactions and are distinguished in charged leptons (l) and neutrinos (ν).
The charged leptons (see Table 2.1) are the electron (e), the muon (μ) and the tau (τ), and have a charge Q/e = -1, where e is the electron charge module.

Name	Symbol	Charge	Spin	Mass(GeV/c^2)
electron	e	-1	1/2	0.511×10^{-3}
muon	μ	-1	1/2	105.7×10^{-3}
tau	τ	-1	1/2	1.78

Table 2.1: Characteristics of charged leptons.

Each charged lepton l is associated with a neutrino ν_l, see Table 2.2, forming a lepton generation.

Neutrino	Symbol	Charge	Spin	Mass(eV/c^2)
electron	ν_e	0	1/2	< 2.2
muon	ν_μ	0	1/2	170×10^3
tau	ν_τ	0	1/2	15.5×10^6

Table 2.2: Characteristics of neutrinos.

For them the SM provides a null mass, even if there are extensions of the SM that consider a mass different from zero, as they indicate experimental evidences.

Name	Symbol	Charge	Spin	Mass(GeV/c^2)
down	d	$-1/3$	$1/2$	$3 \div 7 \times 10^{-3}$
up	u	$+2/3$	$1/2$	$1.5 \div 3 \times 10^{-3}$
strange	s	$-1/3$	$1/2$	$\sim 95 \times 10^{-3}$
charm	c	$+2/3$	$1/2$	~ 1.25
bottom	b	$-1/3$	$1/2$	$4.2 \div 4.7$
top	t	$+2/3$	$1/2$	~ 173

Table 2.3: Characteristics of quarks.

To each lepton is associated a respective anti-lepton with the same mass and with all the opposite quantum numbers.
It is experimentally observed that the difference between number of leptons and numbers of anti-leptons is conserved in each process.
Then the leptonic number L is introduced such that:

- L = +1 for leptons;
- L = -1 for anti-leptons;
- L = 0 for other particles;

and the algebraic sum of L is preserved in each process.
It is also experimentally proven that the conservation of the lepton number is applied separately to electrons, muons and tau.
The quarks (see Table 2.3) are capable of strong, weak and electromagnetic interaction. For each quark there is a corresponding anti-quark with the same mass and all inverted quantum numbers.

Fermions have also a property called chirality, which is determined by whether the particle transforms in a right- or left-handed representation of the Poincaré group, and they can be left-handed (left-chiral) or right-handed (right-chiral). It is experimentally verified that left-handed fermion fields transform differently under some gauge symmetries than right-handed fermion fields. This results in an asymmetry in the properties of fermions, in fact, there are left-handed and right-handed charged leptons, left-handed neutrinos, but no right-handed neutrinos. This does not yet have an explanation from prime principles.

The bosons (see Table 2.4) are the mediators of SM interactions. Each interaction is associated with a set of spin-1 (vector) fields and with an conserved quantum number. The number of the mediator bosons for an interaction is determined by the symmetry group associated with it.

Interaction	Mediators	Charge	Spin	Mass(GeV/c^2)
electromagnetic	γ	0	1	0
weak	W^+, W^-, Z	+1,-1,0	1	80.385 (W), 91.1876 (Z)
strong	8 gluons (g)	0	1	0

Table 2.4: Characteristics of bosons.

The free particle Lagrangian density is requested to be invariant under a local gauge transformation from the symmetry group:

$$SU(3)_C \otimes SU(2)_I \otimes U(1)_Y$$

where:

- the special unitary group $SU(3)_C$ is the symmetry that generates the strong interaction. Its generators are proportional to 3×3 Gell-Mann matrices λ_j (j = 1, ..., 8), the eight associated vector fields are $G_\mu^{1,\dots,8}$ and its conserved quantum number is the color C. Three possible colors are present (red, green and blue). Strong interaction is mediated by an octet of vector bosons, the gluons, that are colored particles themselves;

- the $SU(2)_I \otimes U(1)_Y$ group is the symmetry that generates electromagnetic and weak interactions into an unified theory known as the Glashow-Salam-Weinberg (GSW) model.
  The generators of the special unitary group $SU(2)_C$ are proportional to 2×2 Pauli matrices σ_i (i = 1, 2, 3), the three associated vector fields are $W_\mu^{1,2,3}$ and the conserved quantum number is the observed component I_3 of the weak isospin I.
  The generator of the unitary group $U(1)_Y$ is a unitary scalar complex operator, the associated vector field is B_μ and the conserved quantum number is the weak hypercharg Y.
  The physical mediators generated by this symmetry are the vector bosons $W^\pm$, Z and γ. While the photon is massless, all mediators from weak interactions are massive particles. In order to produce a mass term for $W^\pm$ and Z that does not destroy the gauge invariance for the SM lagrangian, the spontaneous symmetry breaking mechanism is introduced. This mechanism predicts the presence of a scalar particle, the Higgs boson, whose couplings with the vector bosons allow the presence of the required mass term.

2.2 The Quantum Electrodynamics

The quantum electrodynamics (QED) is a quantum field theory which describes how electrically charged particles and matter interact through electromagnetic interaction, including also the theory of special relativity.
Mathematically, QED is an abelian gauge theory with the symmetry group $U(1)_q$ that describes the dynamics and interactions of fermions and the electromagnetic field.
Richard Feynman called it "the jewel of physics" for its extremely accurate predictions of quantities like the anomalous magnetic moment of the electron and the Lamb shift of the energy levels of hydrogen.
The free Lagrangian density for QED ($\mathcal{L}^0_{QED}$) consists of two terms, the free Lagrangian density of the Dirac field ψ ($\mathcal{L}_D$) and the free Lagrangian density of the electromagnetic field ($\mathcal{L}_\gamma$).

$$\mathcal{L}_D = i\bar{\psi}\gamma^\mu\partial_\mu\psi - m\bar{\psi}\psi \tag{2.1}$$

where the first is the kinetic term and the last is a mass term.
In particular m is the fermion mass parameter, γ_μ are the Dirac matrices and ψ ($\bar{\psi}$) is the 4-components spinor field for the fermions (its adjoint).
ψ can be written in term of its chiral components as $\psi = \begin{pmatrix}\psi_R \\ \psi_L\end{pmatrix}$.

$$\mathcal{L}_\gamma = -\frac{1}{4}F^{\mu\nu}F_{\mu\nu} \tag{2.2}$$

where $F_{\mu\nu} = \partial_\mu A_\nu - \partial_\nu A_\mu$ and A_μ is the 4-vector electromagnetic field.
So

$$\mathcal{L}^0_{QED} = \mathcal{L}_D + \mathcal{L}_\gamma = i\bar{\psi}\gamma^\mu\partial_\mu\psi - m\bar{\psi}\psi - \frac{1}{4}F^{\mu\nu}F_{\mu\nu} \tag{2.3}$$

The dynamics equations obtained from 2.3 do not couple the fermion field ψ and the electromagnetic field A_μ, so an additional interaction term is needed, and it is obtained using a gauge invariance principle.
The Lagrangian density 2.3 is invariant under a global $U(1)_q$ gauge transformation, $\psi \longrightarrow \psi' = e^{i\theta}\psi$, where θ is a real constant number, but it is not invariant under a local $U(1)_q$ gauge transformation, $\psi \longrightarrow \psi' = e^{i\theta(x)}\psi$, where $\theta(x)$ has now dependance from the space-time point.
The gauge principle consists in imposing this local $U(1)_q$ invariance.
The interaction term is

$$\mathcal{L}_{int} = -q\bar{\psi}\gamma^\mu A_\mu\psi = -J^\mu A_\mu \tag{2.4}$$

where the quantity J^μ is interpreted as the charge current, that is the probability current of the particle multiplied by its charge, and it can be reabsorbed by a redefinition of the standard derivative with the covariant derivative

$$D_\mu \equiv \partial_\mu - iqA_\mu.$$

While the global gauge invariance leads to the conservation of the electric charge Q, the local gauge invariance leads to the introduction of the vector field A_μ whose gauge boson is the photon γ, which must have zero mass so that the local invariance is not destroyed.
Finally the Lagrangian density for the QED is

$$\mathcal{L}_{QED} = i\bar{\psi}\gamma^\mu\partial_\mu\psi - m\bar{\psi}\psi - \frac{1}{4}F^{\mu\nu}F_{\mu\nu} - q\bar{\psi}\gamma^\mu A_\mu\psi \tag{2.5}$$

where the Lagrangian density is invariant under any $U(1)_q$ transformation and the field transform, under the gauge transformation, as $A_\mu \longrightarrow A_\mu - \frac{1}{q}\partial_\mu\theta(x)$ and $\psi \longrightarrow e^{i\theta(x)}\psi$.

2.3 The Electroweak theory

In 1933, Fermi proposed the first theory of the weak interaction suggesting that beta decay could be explained by a four-fermion interaction, involving a contact force with no range.
The weak interaction is so called because it is normally much less intense than the electromagnetic and strong interactions.
It violates the conservation of parity (P), charge (C), their product (CP) and, for the CPT theorem, we also expect temporal inversion (T).
The processes that involve neutrinos and those that imply a change of flavor in the quarks are certainly weak because the first have neither an electric charge nor a strong charge, while the change of flavor is prohibited both for the electromagnetic interaction and for the strong interaction.
Since the weak interaction is mediated by massive particles (W^+, W^- and Z^0), the interaction range is reduced, $r \sim 10^{-18}m$.
On the basis of the boson which mediates the process, there are processes of a charged current, in which there is the mixing of the flavour, and processes of neutral currents.
In 1968, Glashow, Salam and Weinberg unified the electromagnetic force and the weak interaction by showing them to be two aspects of a single force named the electroweak force.

2.3.1 The GSW model

The GSW model is a quantum field theory based on the symmetry group $SU(2)_L \otimes U(1)_Y$, where L stands for the left-handed chiral components of the fields and it means that only those components take part in the weak interactions.
In this theory the fermions, eigenstates of the weak interaction, are arranged in six doublets of the symmetry of weak isospin $SU(2)_L$.

The six doublets are divided into three doublets for leptons:

$$I = 1/2 \qquad \begin{matrix} I_3 = +1/2 \\ I_3 = -1/2 \end{matrix} \qquad \begin{pmatrix} \nu_e \\ e \end{pmatrix}_L \begin{pmatrix} \nu_\mu \\ \mu \end{pmatrix}_L \begin{pmatrix} \nu_\tau \\ \tau \end{pmatrix}_L \tag{2.6}$$

and three for quarks:

$$I = 1/2 \qquad \begin{matrix} I_3 = +1/2 \\ I_3 = -1/2 \end{matrix} \qquad \begin{pmatrix} u \\ d' \end{pmatrix}_L \begin{pmatrix} c \\ s' \end{pmatrix}_L \begin{pmatrix} t \\ b' \end{pmatrix}_L \tag{2.7}$$

It is important to note that the weak interaction eigenstates *d'*, *s'* and *b'* are obtained as linear combination the strong interaction eigenstates (or mass eigenstates) and the mixing of different flavours is given by

$$\begin{pmatrix} d' \\ s' \\ b' \end{pmatrix} = V \begin{pmatrix} d \\ s \\ b \end{pmatrix}$$

where V is the complex unitary matrix named Cabibbo-Kobayashi-Maskawa (CKM) matrix:

$$V = \begin{pmatrix} V_{ud} & V_{us} & V_{ub} \\ V_{cd} & V_{cs} & V_{cb} \\ V_{td} & V_{ts} & V_{tb} \end{pmatrix}.$$

Also in the GSW model a local gauge transformation invariance is required and the local $SU(2)_L$ gauge transformation acts on the weak isospin in this way:

$$\begin{pmatrix} \nu_l \\ l^- \end{pmatrix}_L^{'} = e^{-\frac{i}{2}\vec{\alpha}(x)\cdot\vec{\tau}} \begin{pmatrix} \nu_l \\ l^- \end{pmatrix}_L,$$

where $\vec{\tau}$ are the Pauli matrices and $\vec{\alpha}(x)$ is the vector of real parameters of the transformation that depends on the space-time coordinates.
Therefore, the left-handed chiral component of fermions contributes to weak processes of charging current, while the right-handed chiral component contributes to weak processes of neutal current, so the latter has the properties of an $SU(2)$ singlet.
The invariance under the $SU(2)_L$ group leads to the introduction of an isospin triplet of Yang-Mills fields named W^1, W^2 and W^3. Two of these can be combined together in order to give two vector bosons $W^\pm$, that are electrically charged and can induce transitions between the members of the weak isospin doublets. The third gauge boson of the triplet should be electrically neutral and this led to the idea of an unification of electromagnetic and weak forces by introducing a new $SU(2)_I \otimes U(1)_Y$ symmetry group.
This symmetry group therefore requires the presence of 3 + 1 gauge fields (W^1, W^2, W^3 for $SU(2)_I$ and B for $U(1)_Y$). The relevant quantum numbers are the hypercharge Y and the weak isospin I.

The Gell-Mann-Nishijima relation allows to define the electromagnetic charge of a particle from the electroweak quantum numbers:

$$Q = I_3 + \frac{Y}{2}.$$

The electroweak Lagrangian density is obtained requiring gauge local invariance under the $SU(2)_I \otimes U(1)_Y$ group that, in a similar way to the electromagnetic case, leads to the introduction of the covariant derivative:

$$D_\mu = \partial_\mu + ig\frac{\vec{\tau}}{2} \cdot \vec{W}_\mu + ig'\frac{Y}{2}B_\mu \tag{2.8}$$

where g and g' are the two coupling constants for the two interactions.
This Lagrangian density includes a Dirac term for fermions

$$\mathcal{L}_{fermions} = \sum_f \bar{\psi} i\gamma^\mu D_\mu \psi, \tag{2.9}$$

neglecting the mass term, and a term for the dynamics of the gauge boson fields

$$\mathcal{L}_{gauge} = -\frac{1}{4}W^{i\mu\nu}W^i_{\mu\nu} - \frac{1}{4}B^{\mu\nu}B_{\mu\nu} \tag{2.10}$$

where

$$W^i_{\mu\nu} = \partial_\mu W^i_\nu - \partial_\nu W^i_\mu - g(\vec{W}_\mu \times \vec{W}_\nu)^i \tag{2.11}$$

$$B_{\mu\nu} = \partial_\mu B_\nu - \partial_\nu B_\mu \tag{2.12}$$

are tensor fields, W^i_μ is one of the three components of the vector field $\vec{W}$ and the term $\vec{W}_\mu \times \vec{W}_\nu$ introduces the coupling of the three gauge bosons W^1, W^2 and W^3.
By combining these informations one has that

$$\begin{aligned}\mathcal{L}_{EW} = {} & \bar{\psi}_L i\gamma^\mu \left(\partial_\mu + ig\frac{\vec{\tau}}{2} \cdot \vec{W}_\mu + ig'\frac{Y}{2}B_\mu\right)\psi_L + \\ & + \bar{\psi}_R i\gamma^\mu \left(\partial_\mu + ig'\frac{Y}{2}B_\mu\right)\psi_R + \\ & - \frac{1}{4}W^{i\mu\nu}W^i_{\mu\nu} - \frac{1}{4}B^{\mu\nu}B_{\mu\nu}\end{aligned} \tag{2.13}$$

where the subscripts L and R indicate the left- and right-handed chiral components of the fermions.
Here the gauge fields are all massless but the vector bosons $W^\pm$ and Z have a non-zero mass, as confirmed by the UA1 and UA2 collaborations. It is therefore necessary to introduce a new term for a boson field, invariant under an $SU(2)_L \otimes U(1)_Y$ transformation, that coherently represents the masses of the particles. This term is generated by the Higgs mechanism in which the introduction of a new scalar particle (the Higgs boson) provides mass.

2.3.2 Higgs mechanism

We introduce a doublet of isospin with a hypercharge Y = 1 of complex scalar fields:

$$\phi = \begin{pmatrix} \phi^+ \\ \phi^0 \end{pmatrix} = \frac{1}{\sqrt{2}} \begin{pmatrix} \phi_1 + i\phi_2 \\ \phi_3 + i\phi_4 \end{pmatrix}, \tag{2.14}$$

where the complex scalar field ϕ^+ destroys positive charged particles and creates negative charged particles and ϕ^0 destroys neutral particles and creates neutral antiparticles.
The Lagrangian density for this field is:

$$\mathcal{L} = (D^\mu \phi)^\dagger D_\mu \phi - V(\phi) = (D^\mu \phi)^\dagger D_\mu \phi - \frac{1}{2}\mu^2 \phi^\dagger \phi - \frac{1}{4}\lambda(\phi^\dagger \phi)^2 \tag{2.15}$$

where $V(\phi)$ is the potential responsible of the symmetry breaking and the parameter λ is assumed to be positive.
If $\mu^2 > 0$, the potential V assumes a unique minimum at $\phi_0 = 0$. Instead, if $\mu^2 < 0$, the shape of the potential is modified, as can be seen in the Figure 2.1, and V assumes a non-trivial minimum at

$$\phi_0^2 = -\frac{\mu^2}{2\lambda} \equiv \frac{v^2}{2},$$

located on a circle of the complex plane $Re(\phi) - Im(\phi)$ of radius v.

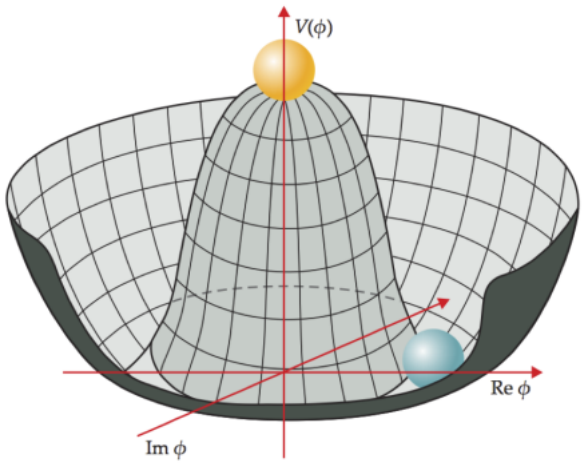

Figure 2.1: Shape of the Higgs potential for $\mu^2 < 0$.

Without any loss of generality the vacuum state can be written:

$$\phi_0 = \frac{1}{\sqrt{2}} \begin{pmatrix} 0 \\ v \end{pmatrix}. \tag{2.16}$$

By the parametrization of the fluctuations of ϕ field around ϕ_0,

$$\phi = \frac{1}{\sqrt{2}} \begin{pmatrix} 0 \\ v + H(x) \end{pmatrix} \tag{2.17}$$

with $v = \sqrt{-\mu^2/\lambda}$ and H(x) is the Higgs scalar field.

The Lagrangian density of the sector of gauge fields plus ϕ field, after the request of local gauge invariance of $SU(2)_L \otimes U(1)_Y$, is:

$$\mathcal{L}_{G\phi} = (D^\mu \phi)^\dagger D_\mu \phi - \frac{1}{2}\mu^2 \phi^\dagger \phi - \frac{1}{4}\lambda(\phi^\dagger \phi)^2 - \frac{1}{4} W^{i\mu\nu} W^i_{\mu\nu} - \frac{1}{4} B^{\mu\nu} B_{\mu\nu} \tag{2.18}$$

By substituting the state 2.17 in the Lagrangian density 2.18, one finds that:

$$\begin{aligned} \mathcal{L}_{G\phi} = & \frac{1}{2}\partial_\mu H \partial^\mu H - \lambda v^2 H^2 + \\ & - \frac{1}{4}(\partial_\mu W^1_\nu - \partial_\nu W^1_\mu)(\partial^\mu W^{1\nu} - \partial^\nu W^{1\mu}) + \frac{1}{8} g^2 v^2 W^1_\mu W^{1\mu} + \\ & - \frac{1}{4}(\partial_\mu W^2_\nu - \partial_\nu W^2_\mu)(\partial^\mu W^{2\nu} - \partial^\nu W^{2\mu}) + \frac{1}{8} g^2 v^2 W^2_\mu W^{2\mu} + \\ & - \frac{1}{4}(\partial_\mu W^3_\nu - \partial_\nu W^3_\mu)(\partial^\mu W^{3\nu} - \partial^\nu W^{3\mu}) - \frac{1}{4} C_{\mu\nu} C^{\mu\nu} + \\ & + \frac{1}{8} v^2 (g W^3_\mu - g' B_\mu)(g W^{3\mu} - g' B^\mu) \end{aligned} \tag{2.19}$$

where the first line is the Lagrangian density of a massive scalar field, the Higgs one, with mass

$$m_H = \sqrt{2\lambda} v = \sqrt{2}|\mu|;$$

the next two lines show that the components W^1_μ and W^2_μ of the triplet $\vec{W}_\mu$ have acquire mass

$$M_1 = M_2 = \frac{1}{2} g v = M_W;$$

the last two lines show that W^3_μ and B_μ field are mixed.
Note that the last line concerns only the combination $gW^3_\mu - g'B_\mu$, which evidently acquires mass. Then we can rearrange the two lines replacing W^3_μ and B_μ with two new fields Z_μ and A_μ obtained as orthogonal combinations of the previous ones:

$$Z_\mu = cos\theta_W W^3_\mu - sin\theta_W B_\mu \tag{2.20}$$

$$A_\mu = sin\theta_W W^3_\mu + cos\theta_W B_\mu \tag{2.21}$$

where θ_W is the Weinberg angle, or weak mixing angle, defined as

$$cos\theta_W = \frac{g}{\sqrt{g^2 + g'^2}}, \qquad sin\theta_W = \frac{g'}{\sqrt{g^2 + g'^2}} \tag{2.22}$$

and experimentally determinable.
In this way the last two lines become:

$$-\frac{1}{4}(\partial_\mu Z_\nu - \partial_\nu Z_\mu)(\partial^\mu Z^\nu - \partial^\nu Z^\mu) + \frac{1}{8}v^2(g^2 + g'^2)Z_\mu Z^\mu - \frac{1}{4}F_{\mu\nu}F^{\mu\nu}$$

with

$$F_{\mu\nu} = \partial_\mu A_\nu - \partial_\nu A_\mu.$$

Thus the field Z_μ has mass

$$M_Z = \frac{1}{2}v\sqrt{g^2 + g'^2} = \frac{M_W}{cos\theta_W}, \tag{2.23}$$

and A_μ continues to be a field with no mass.
If we now write the fields W^3_μ and B_μ in terms of the fields A_μ and Z_μ

$$W^3_\mu = cos\theta_W Z_\mu + sin\theta_W A_\mu \tag{2.24}$$

$$B_\mu = -sin\theta_W Z_\mu + cos\theta_W A_\mu \tag{2.25}$$

and express g' in terms of g

$$g' = gtan\theta_W, \tag{2.26}$$

the covariant derivative present in the Lagrangian density 2.18 assumes the form:

$$\begin{aligned} D_\mu = \partial_\mu + ig\frac{1}{2}[\tau^1 W^1_\mu + \tau^2 W^2_\mu] + igsin\theta_W Q A_\mu + \\ + \frac{ig}{cos\theta_W}\left[\frac{\tau^3}{2} - sin^2\theta_W Q\right] Z_\mu. \end{aligned} \tag{2.27}$$

In order to obtain the correct electromagnetic D_μ, we must identify

$$e = g'cos\theta_W = gsin\theta_W. \tag{2.28}$$

Furthermore, the two combinations

$$W^\pm_\mu = \frac{1}{\sqrt{2}}(W^1_\mu \mp iW^2_\mu) \tag{2.29}$$

can be identified as the fields associated with the physical bosons $W^\pm$, where W^+_μ destroys a W^+ or creates a W^- and W^-_μ does the opposite.

2.3.3 Masses of fermions

Fermion masses can be generated through the spontaneous breaking of the $SU(2)_L \otimes U(1)_Y$ gauge symmetry coupling the fermions to a scalar field that acquires a value of expectation on the vacuum.
Consider a doublet of weak isospin, it is possible to introduce a gauge invariant mass term with a Yukawa coupling between the fermion field ψ and the Higgs field ϕ written as:

$$\mathcal{L}_Y = -g_f(\bar{\psi}_L \phi \psi_R + \bar{\psi}_R \phi^\dagger \psi_L) \tag{2.30}$$

where g_f is the Yukawa coupling constant.

In the case of leptons, by substituting the state 2.17 in the mass term 2.30 one obtains:

$$\begin{aligned} \mathcal{L}_Y &= -\frac{g_f}{\sqrt{2}} \left[(\nu_l, l)_L \begin{pmatrix} 0 \\ v+H \end{pmatrix} l_R + l_R (0, v+H) \begin{pmatrix} \nu_l \\ l \end{pmatrix}_L \right] = \\ &= -\frac{g_f}{\sqrt{2}} (v+H)(l_L l_R + l_R l_L) = \\ &= -\frac{g_f v}{\sqrt{2}} (l_L l_R + l_R l_L) - \frac{g_f}{\sqrt{2}} (l_L l_R + l_R l_L) H \end{aligned} \tag{2.31}$$

the first term represents the coupling of lepton with the Higgs filed and it is a mass term a la Dirac, so it allows to identify the constant coefficient of $(l_L l_R + l_R l_L)$ as the mass term for leptons:

$$m_l = \frac{g_f v}{\sqrt{2}}, \tag{2.32}$$

while the second term represents the coupling of lepton with the Higgs boson.

Since the mass was generated by the lower component of the Higgs doublet, only the lower component of the fermionic doublet receives mass. To generate the masses of the upper member of the weak isospin doublet, the conjugate Higgs doublet must be introduced.
In the case of leptons, the right-handed component of the neutrino would appear that, according to the SM, it does not exist, so the neutrino mass is zero.
The quarks, instead, have both a right-handed and a left-handed component, so:

$$\begin{aligned} \mathcal{L}_Y &= -\frac{1}{\sqrt{2}} \left[g^d_{ij} (u_i, d_i)_L \begin{pmatrix} 0 \\ v+H \end{pmatrix} d_{jR} + g^u_{ij} (u_i, d_i)_L \begin{pmatrix} -(v+H)^* \\ 0 \end{pmatrix} u_{jR} + h.c. \right] = \\ &= -\frac{1}{\sqrt{2}} (v+H) \left[g^u_{ij} u_{iL} u_{jR} + g^d_{ij} d_{iL} d_{jR} + h.c. \right] \end{aligned} \tag{2.33}$$

with u_i = (u, c, t) and d_i = (d, s, b), and the mass terms are:

$$m^u_{ij} = -\frac{v}{\sqrt{2}} g^u_{ij} \qquad\qquad m^d_{ij} = -\frac{v}{\sqrt{2}} g^d_{ij} \tag{2.34}$$

The mass terms m^u and m^d are not diagonal in this basis but they can be made diagonal with four different transformations on the triplets u_{iL}, u_{iR}, d_{iL} and d_{iR} through:

$$u_{\alpha L} = (U^u_L)_{\alpha i} u_{iL} \quad u_{\alpha R} = (U^u_R)_{\alpha i} u_{iR} \quad d_{\alpha L} = (U^d_L)_{\alpha i} d_{iL} \quad d_{\alpha R} = (U^d_R)_{\alpha i} d_{iR} \tag{2.35}$$

where α is the index in the mass diagonal basis and i is the index in the non-diagonal weak interaction basis.
The 2.33 becomes:

$$\mathcal{L}_Y = \left(1 + \frac{H}{v}\right) [m^u u\bar{u} + m^d d\bar{d} + m^s s\bar{s} + m^c c\bar{c} + m^t t\bar{t} + m^b b\bar{b}]. \tag{2.36}$$

Even if this kind of Yukawa coupling solves the problem of fermions' masses, it does not arise from a gauge principle and it is purely phenomenological and needs a specific coupling constant for each fermion-Higgs interaction. Moreover the couplings are very different given the wide range of fermion masses experimentally observed.

If we now consider the electroweak Lagrangian density and substitute the eigenkets of the weak interaction with the mass ones, we see that the term of the coupling with the Z boson, i.e. neutral current coupling term, is diagonal also in the mass basis if the matrices U in the transformations 2.35 are unitary, instead the term of the coupling with the W boson, i.e. charged current coupling term, is:

$$\begin{aligned} \mathcal{L}_{CC} &= -\frac{g}{\sqrt{2}} (\bar{u}_i, \bar{d}_i)_L \gamma^\mu \tau_+ W^+_\mu \begin{pmatrix} u_i \\ d_i \end{pmatrix}_L + h.c. = \\ &= -\frac{g}{\sqrt{2}} \bar{u}_{iL} \gamma^\mu d_{iL} W^+_\mu + h.c. = \\ &= -\frac{g}{\sqrt{2}} \bar{u}_{\alpha L} [(U^u_L)_{\alpha i} (U^d_L)^\dagger_{\beta i}] \gamma^\mu d_{\beta L} W^+_\mu + h.c. \end{aligned} \tag{2.37}$$

where

$$V_{\alpha\beta} = [U^u_L U^{d\dagger}_L]_{\alpha\beta} \tag{2.38}$$

is the 3×3 matrix CKM, unitary but not diagonal. It displays the mismatch between the weak eigenstates and the mass eigenstates and leads to transitions between quark generations through flavour changing interactions.

2.4 Quantum chromodynamics

The quantum chromodynamics (QCD) is a quantum field theory which describes the strong interaction between quarks.
Mathematically, QCD is a non-abelian gauge theory based on the symmetry group $SU(3)_C$ where the subscript C stands for the charge associated with this symmetry, named color and it has three possible states labelled as red, green and blue.
This theory is invariant under the local $SU(3)_C$ transformation

$$\psi \longrightarrow \psi' = e^{ig_s\vec{\alpha}(x)\cdot\vec{T}}\psi \tag{2.39}$$

where g_s is the strong coupling costant, $\vec{\alpha}(x)$ are eight functions of the space-time coordinate x and $\vec{T} = T^\alpha$ are the eight generators of the symmetry group. Those generators are related to the Gell-Mann matrices:

$$T^\alpha = \frac{1}{2}\lambda^\alpha \tag{2.40}$$

and follow the commutation rule

$$[T_\alpha, T_\beta] = if_{\alpha\beta\gamma}T_\gamma \tag{2.41}$$

where $f_{\alpha\beta\gamma}$ are the structure constants of the group $SU(3)_C$ and the indices run from 1 to 8.

The Lagrangian density of free quarks, assuming massless quarks, is

$$\mathcal{L} = \sum_{f=1}^{6} \bar{\psi}^f i\gamma^\mu \partial_\mu \psi^f \tag{2.42}$$

The local gauge invariance under $SU(3)_C$ introduces 8 massless fields of gauge, gluons, and the covariant derivative D_μ given by

$$D_\mu = \partial_\mu + ig_s T_\alpha G^\alpha_\mu \tag{2.43}$$

where G^α_μ are the 8 gluon fields that transform as

$$G^\alpha_\mu \longrightarrow G'^\alpha_\mu = G^\alpha_\mu + ig_s f^{\alpha\beta\gamma}\theta_b(x)G_{\gamma,\mu}. \tag{2.44}$$

By adding the contribution of the kinetic energy for each gluon, one obtains the complete Lagrangian density for the QCD:

$$\mathcal{L}_{QCD} = \bar{\psi}\gamma^\mu\partial_\mu\psi - m\bar{\psi}\psi - ig_s\bar{\psi}\gamma^\mu\lambda_\alpha\psi G^\alpha_\mu - \frac{1}{4}G^{\mu\nu}_\alpha G^\alpha_{\mu\nu} \tag{2.45}$$

with $G^{\mu\nu}_\alpha$ the tensor field defined as

$$G^{\mu\nu}_\alpha = \partial^\mu G^\nu_\alpha - \partial^\nu G^\mu_\alpha - g_s f_{\alpha\beta\gamma}G^{\beta,\mu}G^{\gamma,\nu}. \tag{2.46}$$

The last term in 2.46 is quadratic in the gluon fields and produces a self-interaction between the gluon fields due to the non-abelian nature of the symmetry group.

The QCD theory exhibits two relevant properties which stem from experimental evidence: the color confinement and the asymptotic freedom.
The quarks are bound together to form hadrons, but no color multiplicity of mass degenerate hadrons is observed, so stable states can only be color singlets and the quarks combine to form no-colored hadrons. This property is known as color confinement.
The study of bound states in QCD presents several difficulties, due to the strength of the coupling that makes a perturbative approach to calculations impossible, but all experimental results show that, for sufficiently high energy processes, quarks inside protons behave as free particles. This property is known as asymptotic freedom and it can be qualitatively explained thanks to the renormalization of QCD theory.

2.5 Unsolved issues in the Standard Model

Despite the great successes of MS, such as the prediction of the existence of the Higgs boson, which is the last experimental validation of the electroweak theory, this model fails to give an explanation of many other phenomena and, as of today, some notable problems are still unresolved.

- **Large set of parameters.** In the SM there are many parameters that are not postulated by theory and must therefore be obtained via measurements:
  - fermion mass;
  - mass of Higgs boson;
  - CKM matrix elements;
  - coupling constants (g, g' and g_s).
- **Hierarchy in fermion masses.** There is no explanation or prediction of fermion masses that occur in a hierarchical pattern which varies over 5 order of magnitudes between the top quark and the electron, and many orders of magnitude lighter for neutrinos.
- **Higgs mass fine tuning.** The Higgs mass receives radiative corrections through bosonic and fermionic loops. Self-interaction terms arise such as
$$m_H^2 \approx M_{H,0}^2 + \frac{\lambda}{4\pi^2}\Lambda^2$$
where $M_{H,0}$ is the bare mass of the Higgs, λ is the strength of the coupling and Λ^2 is the scale of new physics. Since the Higgs boson has

to couple to every massive particle, one can recalculate the one-loop corrections to Higgs mass as:

$$m_H^2 \approx M_{H,0}^2 + \frac{g_f}{4\pi^2}(\Lambda^2 + m_f^2) + \frac{g_s}{4\pi^2}(\Lambda^2 + m_s^2)$$

with g_f and g_s the coupling constant of fermions and scalar particles to the Higgs and m_f and m_s the related mass term. These corrections are quadratically divergent with the cut-off (that represents the scale beyond which new physics needs to be considered). Usually, a typical scale is the Planck scale where the corrections are $\sim 10^{30} m_H^2$, many orders of magnitude larger than the Higgs mass at tree level. A precise tuning between fermions and scalars, known as fine tuning, is required in order to reduce or cancel this divergences.

- **Electroweak unification.** The GWS model cannot be considered a real unification theory because the symmetry group is the product of two different groups each one with its own constant, g and g' not linked by the theory, so the ratio $g'/g = tan\theta_W$ has to be determined experimentally.

- **Neutrino sector.** The SM assumes neutrinos to be massless, while observations of flavour oscillations can only be explained by massive neutrinos, via a mixing of the electroweak eigenstates.

- **Symmetries and conservation.** There are some experimental facts that have to be inserted ad hoc in the theory (such as electrical charge quantization, the proton stability and the conservation of the baryonic number) while other ones come from a symmetry.

- **Matter-antimatter asymmetry.** The only SM CP-violation in the quark sector is not sufficient to justify the actual matter-antimatter asymmetry measured in the universe.

- **Gravity.** The SM does not include in any way General Relativity.

- **Dark matter and dark energy.** From astrophysical observations it is found that the orbits followed by galaxies are different from which expected considering the gravitational effects of the usual matter; it could be explained with the existence of an amount of extra matter not composed of known SM particles: this matter is referred to with the name of dark matter. Astronomical evidences show that the universe is made up for the 5% of ordinary matter, while the dark matter should represent the 24%. The remaining 71% is made up of a unknown form of energy, the dark energy. The existence of the dark energy would account for the accelerating expansion of the universe.

Chapter 3

New physics models and W' boson

There are many problems unsolved in the SM and, taking into account the experimental results obtained up to now, we can think that this model is only a good approximation of a more general theory that also incorporates gravitational interaction.
Many theoretical models of physics beyond the SM have already been developed following, mainly, one of these three roads:

- consider the known fundamental fields and introduce new interactions, road which leads to Great Unification, Supersymmetry, string theory;
- consider new fundamental fields with new interactions, as in the case of "compositeness", i.e. that some of the known particles might be composites of other, fundamental, objects;
- use more exotic methods like considering the existence of "large extra dimensions" and that some of these are in the energy range of high-energy.

Many theories that extend the SM predict additional charged gauge bosons, often referred to as W' bosons. Some of these theories are:

- **Extra Dimensions Theories**[22]**.** To unify the fundamental forces, extra dimensions are proposed beyond the typical space-time (3+1). The first theory was the Kaluza-Klein theory, a unified field theory of gravitation and electromagnetism built around the idea of a fifth dimension beyond the usual four of space and time and considered an important precursor to string theory. Kaluza detailed a purely classical extension of general relativity to five dimensions, while Klein gave Kaluza's classical five-dimensional theory a quantum interpretation. Klein introduced the hypothesis that the fifth dimension was curled

up and microscopic and suggested that the geometry of the extra fifth dimension could take the form of a circle, with the radius of 10^{-30} cm.
A different approach was given by Arkani-Hamed, Dimopoulos and Dvali (ADD), they showed that the weakness of gravity could be explained by postulating two or more extra dimensions in which only gravity could propagate. The size of these extra dimensions should range between roughly a millimeter and $\sim$1/TeV.
Randall and Sundrum (RS) found a new possibility using a warped geometry, postulating a five-dimensional Anti-de Sitter (AdS) space-time[1] with a compactification scale of order TeV.
The *Large Extra Dimension Theory*, mostly motivated by the ADD model, requires that the fields of the SM are confined to a four-dimensional membrane, while gravity propagates in several additional spatial dimensions that are large compared to the Planck scale.
The *Warped Extra Dimensions*, such as those proposed by the Randall-Sundrum model (RS), are based on warped geometry where the universe is a five-dimensional anti-de Sitter space and the elementary particles, except for the graviton, are localized on a (3+1)-dimensional brane[2] or branes.
The *String Theory* requires extra dimensions for mathematical consistency. Space-time is 26-dimensional in bosonic string theory, 10-dimensional in superstring theory, and 11-dimensional in supergravity theory and M-theory.

- **Composite Higgs Model.** Many theories propose that particles currently considered as elementary are made up of other, yet unknown, constituents which are strongly coupled forming new heavy resonance. The Composite Higgs Model (CHM) is one of the composite theories and it takes into account that the Higgs boson is a bound state of new strong interactions, so the Higgs boson is not an elementary particle but has finite size, typically around 10^{-18} m. Microscopically the composite Higgs will be made of smaller constituents in the same way as nuclei are made protons and neutrons.
  The main prediction of CHM are new particles with mass around a TeV that are excitations of the composite Higgs[23].
  Within the most compelling scenarios each SM particle has a partner with equal quantum numbers but heavier mass. For example, the γ, W and Z bosons have heavy replicas with mass determined by the compositeness scale, expected around TeV.

[1] In mathematics and physics, n-dimensional anti-de Sitter space (AdS_n) is a maximally symmetric Lorentzian manifold with constant negative scalar curvature.

[2] A brane is a physical object that generalizes the notion of a point particle to higher dimensions. Branes are dynamical objects which can propagate through space-time according to the rules of quantum mechanics. They have mass and can have other attributes such as charge.

CHM is motivated by naturalness problem, the difficulty to explain the different energy scales that appear in the fundamental interactions of particle physics, in particular, the large difference between the mass of the Higgs boson and the Planck scale. CHM can solve the naturalness problem because the Higgs boson is not an elementary particle so that a new energy scale exists that can be explained dynamically similarly to the mass of the proton[24].

- **Little Higgs Model**[25]**.** In particle physics, Little Higgs Models (LHM) are based on the idea that the Higgs boson is a pseudo-Goldstone boson arising from some global symmetry breaking at a TeV energy scale. The main goal of LHM is to use the spontaneous breaking of such approximate global symmetries to stabilize the mass of the Higgs boson responsible for electroweak symmetry breaking.
  In the SM the Higgs mass suffers from an instability under radiative corrections, the LHM offer a new and very promising solution to this problem in which the Higgs is naturally light as a result of non-linearly realized symmetries. In these models, the gauge group has the form of a direct product of several copies of the same factor, for example $SU(2) \otimes SU(2)$. Each $SU(2)$ factor may be visualised as the $SU(2)$ group living at a particular point along an additional dimension of space.

- **Left-Right Symmetry**[26]**.** At current energies the SM contains an $SU(2)_L$ group, i.e the world is left-handed. Left-right symmetry at some larger scale implies the need for an $SU(2)_R$ group, thus right-handed Z, $W^{\pm}$ and ν are introduced too.
  The Higgs fields have to be in a triplet representation, leading to doubly-charged Higgs particles, one set for each of the two $SU(2)$ groups. Also the number of neutral and singly-charged Higgs states is increased relative to the SM.
  The $W_R^{\pm}$ has been implemented as a simple copy of the ordinary $W^{\pm}$, with the exception that it couples to right-handed neutrinos instead of the ordinary left-handed ones. Thus the standard CKM matrix is used in the quark sector, and the same vector and axial coupling strengths, leaving only the mass as free parameter.

- **Sequential Standard Model (SSM)**[27]**.** It predicts the existence of a new massive W'_{SSM} boson with couplings to fermions that are identical to those of the SM W boson, i.e. with final states consisting either of a charged lepton and neutrino or a quark pair, and assumes ν from W' decay to be light and stable. This model represents a good benchmark as the results can be interpreted in the context of other models of new physics, and is useful for comparing the sensitivity of different experiments.

3.1 W' boson

The W' boson is a hypothetical gauge boson that arises from extensions of the electroweak symmetry of the SM. Its name derives from the fact that it is a heavy partner of the SM W boson.
The W' boson, whose there is no evidence at up to now, has spin 1 and electric charge ± 1 and it can be detected directly with proton-proton collisions at the LHC in its leptonic dacay channel ($W' \longrightarrow l\nu_l$) or in its hadronic dacay channel ($W' \longrightarrow$ tb), or indirectly through its effects on low-energy processes, such as muon decay where it can replace the W boson of the SM.

3.1.1 W' couplings to fermions

The lowest dimension Lagrangian density that describes the $W'^{(+)}$ boson couplings to fermions can be written as[28]:

$$\mathcal{L} = \frac{W'^{(+)}_{\mu}}{\sqrt{2}} \left[\bar{q}_i \left(C^R_{qij} P_R + C^L_{qij} P_L \right) \gamma^{\mu} q_j + \bar{\nu}_i \left(C^R_{lij} P_R + C^L_{lij} P_L \right) \gamma^{\mu} l_j \right] \quad (3.1)$$

where q, l and ν (respectively quark, lepton and neutrino) are the SM fermions in the mass eigenstate basis, i, j = 1, 2, 3 label the fermion generation, $P_{R,L} = (1 \pm \gamma_5)/2$ and the coefficients C^R_{qij} , C^L_{qij} , C^R_{lij}, C^L_{lij} are complex dimensionless parameters.
If $C^R_{lij} \neq 0$, the i-th generation includes a right-handed neutrino.

In many theories, the W' boson is associated with a spontaneously broken gauge symmetry and it is often arised in models with an extra $SU(2)$ gauge group, so it is generically accompanied by a Z' boson of almost the same mass; the Z'-to-W' mass ratio is often a free parameter. The simplest extension of the electroweak gauge group that includes a W' boson is $SU(2)_1 \otimes SU(2)_2 \otimes U(1)$. Generally, we might have n copies of $SU(2)$, which are then broken down to a diagonal $SU(2)_W$, which corresponds to the electroweak $SU(2)$; this gives rise to $W'^{(+)}$, $W'^{(-)}$ and Z' bosons. In order for the W' bosons couple to weak isospin, the extra $SU(2)$ and the SM $SU(2)$ must mix; one copy of SU(2) must break around the TeV scale (to get W' bosons with a TeV mass) leaving a second $SU(2)$ for the SM.
In theories in which a tree-level mass mixing is induced between the electrically charged gauge bosons, the diagonalization of the mass matrix leads to $W - Z$ mass ratio and the couplings of the observed W boson different from the SM values; this implies that the $W - W'$ mixing angle, θ_+, must be smaller than about 10^{-2} and, similarly, a $Z - Z'$ mixing must be.
In models based on the "left-right symmetric" gauge group, the SM fermions that couple to the W boson transform as doublets under $SU(2)_L$ while the other fermions transform as doublets under $SU(2)_R$. This brings that the W' boson couples primarily to right-handed fermions and its coupling to

left-handed fermions arises due to the mixing angle θ_+; consequently, C_q^L is proportional to the CKM matrix and its elements are much smaller than the diagonal elements of C_q^R that, generically, is not proportional to V_{CKM}.
In the "alternate left-right"model, all the couplings shown in equation 3.1 vanish, but there are some new fermions such that the W' boson couples to pairs involving a SM fermion and a new fermion.
In the "ununified SM", the left-handed quarks are doublets under one $SU(2)$, and the left-handed leptons are doublets under a different $SU(2)$, leading to a mostly leptophobic W' boson: $C_{lij}^L \ll C_{qij}^L$ and $C_{lij}^R = C_{qij}^R = 0$.
Fermions of different generations may also transform as doublets under different $SU(2)$ gauge groups. In particular, the couplings to third generation quarks may be enhanced.
It is also possible that the W' couplings to SM fermions are highly suppressed. For example, if the quarks and leptons are singlets under one $SU(2)$, then the couplings are proportional to the tiny mixing angle θ_+. Similar suppressions may arise if some vector-like fermions[3] mix with the SM fermions.

3.1.2 Collider searches

At hadron colliders W' bosons can be detected through resonant pair production of fermions or electroweak bosons: searches for a high-mass W' boson resonance have been performed at the Tevatron and the LHC in the lepton-neutrino, diboson and diquark final states.

Assuming that the W' width is much smaller than its mass, the contribution of the s-channel W' boson exchange to the total rate for $pp \longrightarrow f\bar{f}'X$, where f and f' are fermions whose electric charges differ by ± 1 and X is any final state, may be approximated by the branching ratio $Br(W' \longrightarrow f\bar{f}')$ times the production cross section

$$\sigma(pp \longrightarrow W'X) \simeq \frac{\pi}{48s} \sum_{i,j} \left[(C_{qij}^L)^2 + (C_{qij}^R)^2 \right] w_{ij}(M_{W'}^2/s, M_{W'})$$

where the functions w_{ij} include the information about proton structure, and are given to leading order in α_s by

$$w_{ij}(z,\mu) = \int_z^1 \frac{dx}{x} \left[u_i(x,\mu)\bar{d}_j\left(\frac{z}{x},\mu\right) + \bar{u}_i(x,\mu)d_j\left(\frac{z}{x},\mu\right) \right]$$

[3]Vector-like quarks and leptons are hypothetical new fermions that transform in non-chiral representations of the unbroken SM gauge group. Vector-like fermions can have electroweak singlet masses that dominate over the contributions to their masses from Yukawa couplings to the Higgs boson. This means that their loop-induced contributions to precision electroweak observables and radiative Higgs decays and production obey decoupling with large masses.

where $u_i(x,\mu)$ and $d_i(x,\mu)$ are the parton distributions inside the proton, at the factorization scale μ and parton momentum fraction x, for the up- and down-type quark of the i-th generation, respectively. QCD corrections to W' production are sizable (they also include quark-gluon initial states), but preserve the above factorization of couplings at next-to-leading order.

The most commonly studied W' signal consists of a high-momentum electron or muon and large missing transverse momentum, with the transverse mass distribution forming a Jacobian peak with its endpoint at $M_{W'}$.
The branching ratios for $W' \longrightarrow e\nu$ and $W' \longrightarrow \mu\nu$ could be very different, so the results in these channels should be presented separately.
For right-handed W' bosons, the leptonic decays necessarily produce right-handed neutrinos. When the mass of the ν_R is larger than that of the W'_R boson ($M_{W'_R} < M_{\nu_R}$) then the $W'_R \longrightarrow l\nu_R$ decays are kinematically forbidden and only $W'_R \longrightarrow q\bar{q'}$ decays are allowed (of which $W'_R \longrightarrow$ tb is a subset). On the other hand, if the ν_R is lighter than the W'_R boson ($M_{W'_R} > M_{\nu_R}$) then $W'_R \longrightarrow l\nu_R$ decays are allowed.
Then, searches in the channels $W' \longrightarrow e\nu$ and $W' \longrightarrow \mu\nu$ often implicitly assume that the left-handed couplings vanish (no interference between W and W'), and that the right-handed neutrino is light compared to the W' boson and escapes the detector. The W' decay into a lepton and a right-handed neutrino may also be followed by the ν_R decay through a virtual W' boson into a lepton and two quark jets.
A search for new heavy W' bosons decaying to an electron or muon and a neutrino using proton-proton collision data at a centre of mass energy of $\sqrt{s}$ = 13 TeV, with the data set collected in 2015 and 2016 by the ATLAS experiment at the LHC and corresponded to an integrated luminosity of 36.1 fb^{-1}, observed no excess of events above the SM prediction[29]. The results are used to set upper limits on the W' boson cross-section times branching ratio to an electron or muon and a neutrino as a function of the W' mass. Assuming a W' boson with the same couplings as the SM W boson, W' masses below 5.1 TeV are excluded by the combination of the electron and muon channels at the 95% confidence level.
The Figure 3.1 shows the 95% CL upper limits on $\sigma \times BR$ separately for the electron and muon channels and for the combination of the two channels.
A similar analysis was also made with the data set collected in 2015 by the CMS experiment at the LHC and corresponded to an integrated luminosity of 2.3 fb^{-1}[30]. No evidence of an excess of events relative to the SM expectations was observed. Assuming a W' boson with the same couplings as the SM W boson, W' masses below 4.1 TeV are excluded by the combination of the electron and muon channels at the 95% confidence level.
The Figure 3.2 shows the 95% CL upper limits on $\sigma \times BR$ separately for the electron and muon channels and for the combination of the two channels.

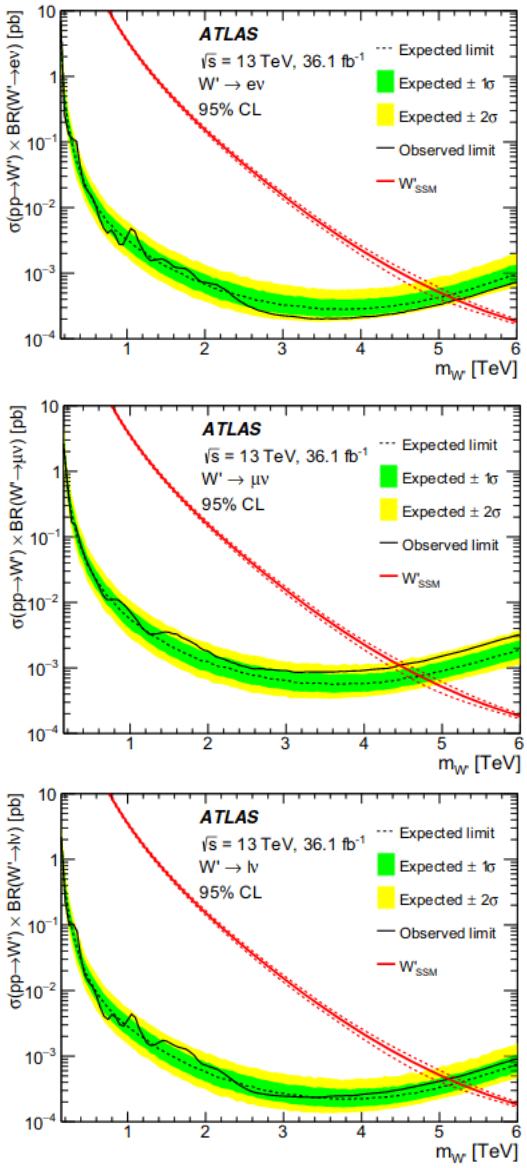

Figure 3.1: Observed (solid black line) and expected (dashed black line) 95% CL upper limits on cross-section times branching ratio ($\sigma \times BR$) as a function of the SSM W' boson mass in the electron (top), muon (center) and combined electron and muon (bottom) decay channels. The 1σ (1 standard deviation, green) and 2σ (2 standard deviation, yellow) expected limit bands are also shown. The predicted $\sigma \times BR$ for SSM W' production is shown as a red solid line.

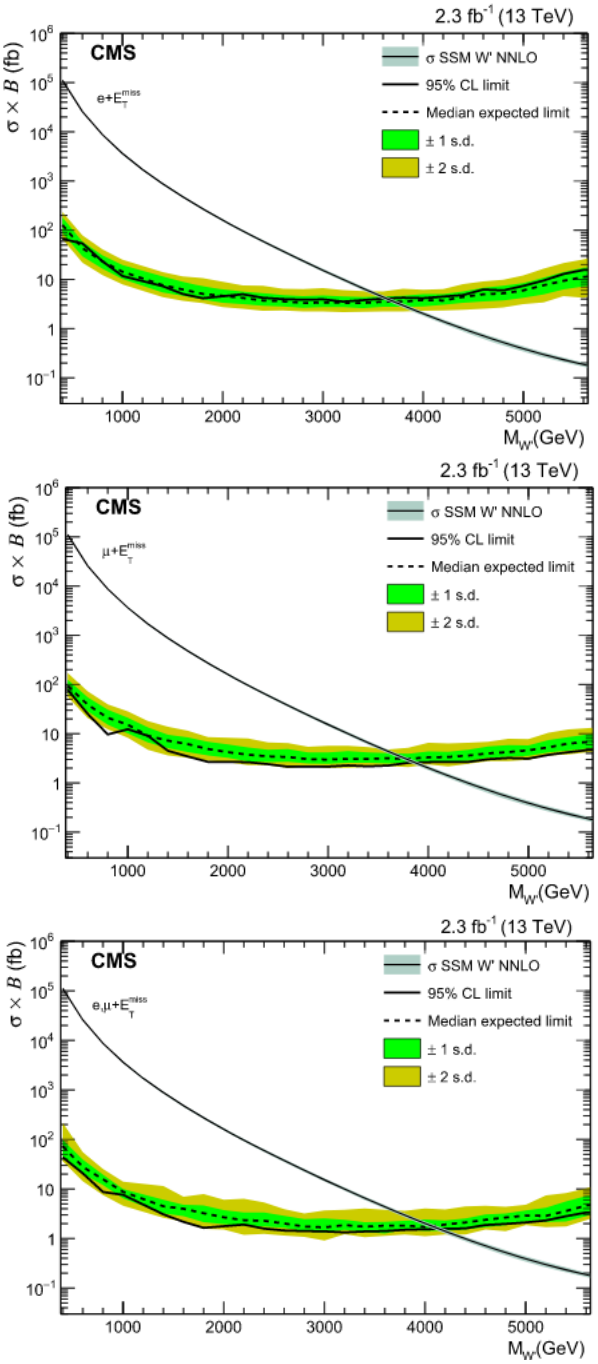

Figure 3.2: Observed (solid black line) and expected (dashed black line) 95% CL upper limits on cross-section times branching ratio ($\sigma \times BR$) as a function of the SSM W' boson mass in the electron (top), muon (center) and combined electron and muon (bottom) decay channels. The 1 s.d. (1 standard deviation, green) and 2 s.d. (2 standard deviation, yellow) expected limit bands are also shown. The predicted $\sigma \times BR$ for SSM W' production is shown as a blue solid line.

The coupling limits are much weaker for $M_{W'} < 150$ GeV, a range last explored with the Tevatron at $\sqrt{s} = 1.8$ TeV[31].

In models where the resonance is sufficiently massive, it is common to postulate that the coupling to third generation quarks might be enhanced relative to the second and first generations, making a search for the decay $W' \longrightarrow$ tb highly appropriate. The usual signature consists of a leptonically decaying W boson and two b-jets.
A search for a heavy W' boson resonance decaying to a top quark and a bottom quark has been performed in lepton + jets final states using data collected at $\sqrt{s} = 13$ TeV by the CMS detector in 2016, corresponding to an integrated luminosity of 35.9 fb^{-1}[32]. No evidenceis observed for the production of a W' boson, and 95% CL upper limits on the product of the right-handed W' (W'_R) boson production cross section and its branching ratio to a top and a bottom quark are calculated as a function of the W'_R boson mass. The observed (expected) 95% CL upper limit is 3.4 (3.3) TeV if $M_{W'_R} >> M_{\nu_R}$ and 3.6 (3.5) TeV if $M_{W'_R} < M_{\nu_R}$, where M_{ν_R} is the mass of the right-handed neutrino. Exclusion limits are also presented for W' bosons with varied left- and right-handed couplings to fermions, for the first time at $\sqrt{s}$ =13 TeV. These results are the most stringent limits to date on the production of W' bosons that decay to a top and a bottom quark.
The Figure 3.3 shows the 95% CL upper limits on $\sigma \times BR$ separately for the electron and muon channels and for the combination of the two channels, while the Figure 3.4 shows the expected (left) and observed (right) limits on the W' boson mass as function of the left-handed (a_L) and right-handed (a_R) couplings.
For lower masses, the best limits on W' couplings to quarks have been set by CMS [33] in the 500-800 GeV range.
Recent studies have also incorporated the fully hadronic decay channel for $M_{W'} \gg m_t$ with the use of jet substructure techniques to tag highly boosted top-jets.

In some theories the W' couplings to SM fermions are suppressed by discrete symmetries. W' production then occurs in pairs, through a photon or Z boson. The decay modes are model-dependent and often involve other new particles. The ensuing collider signals arise from cascade decays and typically include missing transverse momentum.
A fermiophobic W' boson that couples to WZ may be produced at hadron colliders in association with a Z boson, or via WZ fusion. This would give rise to $(WZ)Z$ and $(WZ)jj$ final states, where the parentheses represent a resonance.
W' bosons have also been searched for recently in final states with a W boson and a SM Higgs boson in the channels $W \longrightarrow l\nu$ or $W \longrightarrow qq$ and $h^0 \longrightarrow b\bar{b}$ or $h^0 \longrightarrow WW$.

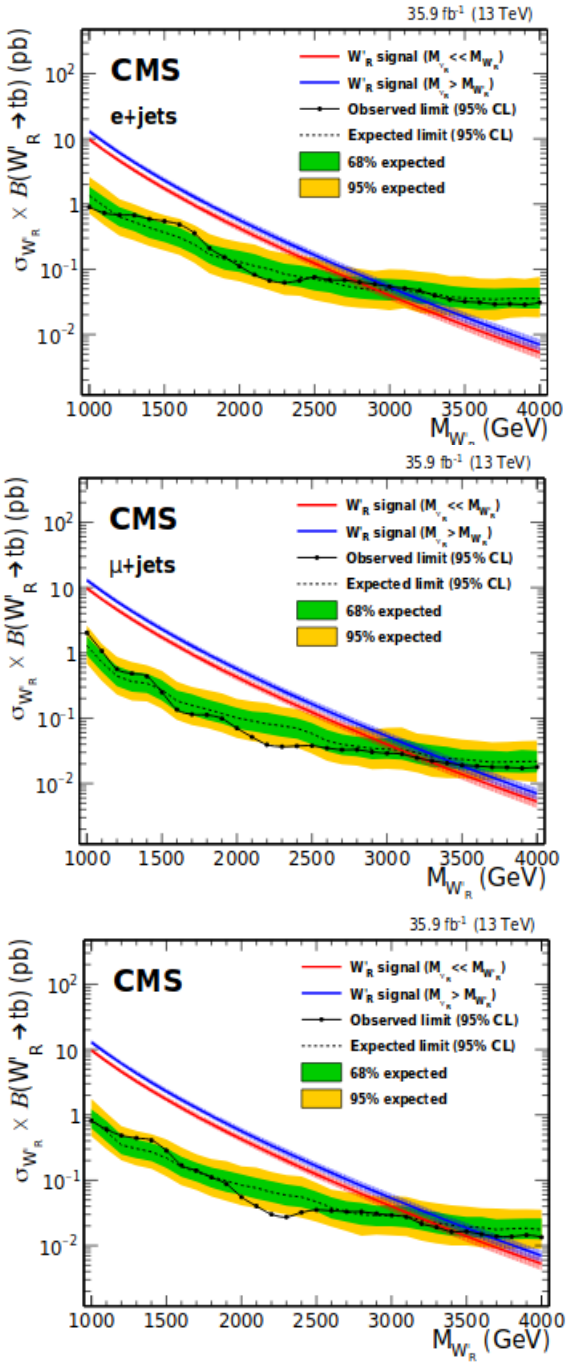

Figure 3.3: Observed (solid black line) and expected (dashed black line) 95% CL upper limits on the W'_R boson cross-section times branching ratio ($\sigma \times BR$) in the electron (top), muon (center) and combined electron and muon (bottom) decay channels. The 1 s.d. (1 standard deviation, green) and 2 s.d. (2 standard deviation, yellow) expected limit bands are also shown. The predicted $\sigma \times BR$ for W'_R production is shown as a red solid line for $M_{W'_R} >> M_{\nu_R}$ and a blue solid line for $M_{W'_R} < M_{\nu_R}$.

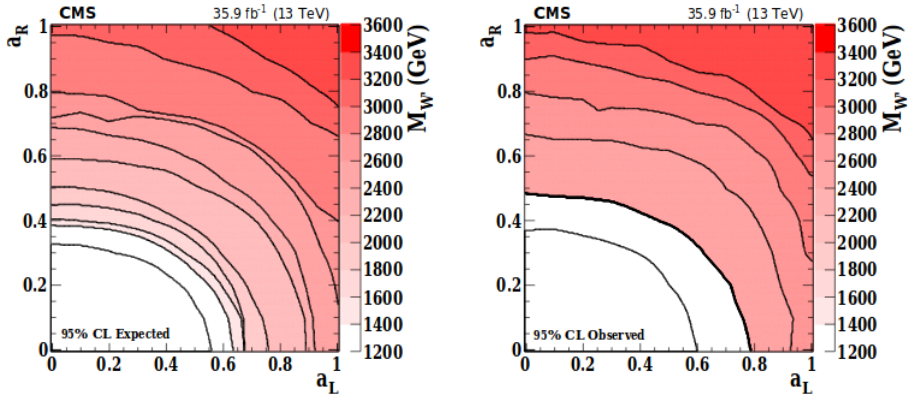

Figure 3.4: Expected (left) and observed (right) limits on the W' boson mass as function of the left-handed (a_L) and right-handed (a_R) couplings. Black lines represent contours of equal W' boson mass separated by 200 GeV.

3.1.3 Low-energy constraints

The properties of W' bosons are also constrained by measurements of processes at energies much below $M_{W'}$ and they are strongly model-dependent. If right-handed neutrinos have Majorana masses, then there are tree-level contributions to neutrinoless double-beta decay, and a limit on $M_{W'}$ versus the ν_R mass may be derived. For ν_R masses below a few GeV, the W' boson contributes to leptonic and semileptonic B meson decays, so that limits may be placed on various combinations of W' parameters. For ν_R masses below ~ 30 MeV, the most stringent constraints on $M_{W'}$ are due to the limits on ν_R emission from supernovae.

Chapter 4

Signal characterization, final state and physical objects of interest

The aim of this thesis work is the search for a new W' resonance using 35.872 fb^{-1} of proton-proton collision data delivered by the LHC at a centre of mass energy of $\sqrt{s}$ = 13 TeV and collected by the CMS experiment in 2016.
The search is performed in the fully hadronic decay channel ($W' \longrightarrow$ tb) where the final state is characterized by the presence of two jets, one produced by the top quark and the other by the b quark.
In the kinematic region of interest, dictated by the W' candidate masses sought after in the region above 1 TeV, the top quark is highly energetic and, due to the Lorentz boost, the angular separation between the top quark decay products (W boson and b quark) is small. The final state particles, resulting from the hadronization of b quark and the decay of W boson into light quarks, usually overlap resulting in a single jet, called *top-jet*. Dedicated methods are applied to resolve the substructure of this top-jet, allowing to strongly suppress background processes not featuring a top quark in the final state. Applying b-jet identification algorithms (b-tagging) to the b-jet from the W' decay, the SM background can be further reduced [34].
The SM processes that contribute significantly to the background for this s-channel decay are:

- $t\bar{t}$, processes where a $t\bar{t}$ quark pair is produced by strong interaction. In particular, if at least one top quark decay hadronically, this can be exchanged for the top quark produced by the W' and the other, if its decay is not well reconstructed, can be mis-identified with a b quark jet produced by the W' decay.

- *QCD multijet*, strong interaction processes in which quarks are pro-

duced. In this case, the final state has two jets, just like the signal. Furthermore, if the quarks produced are b quarks, one of them can mimic the b-tagged jet coming from the top quark, while the other one can occasionally be mis-tagged as a top-jet.

The Feynman diagram of the signal process is shown in Figure 4.1, while in Figure 4.2 there are the Feynman diagrams for $t\bar{t}$ and QCD multijet backgrounds.

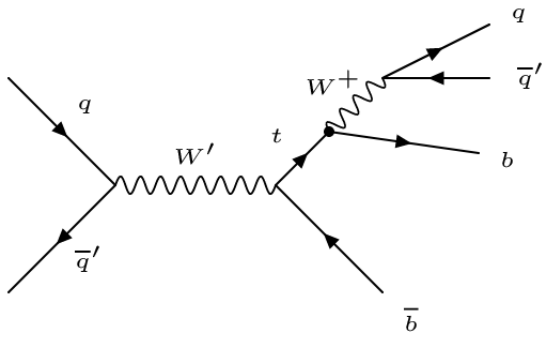

Figure 4.1: Feynman diagram for the signal.

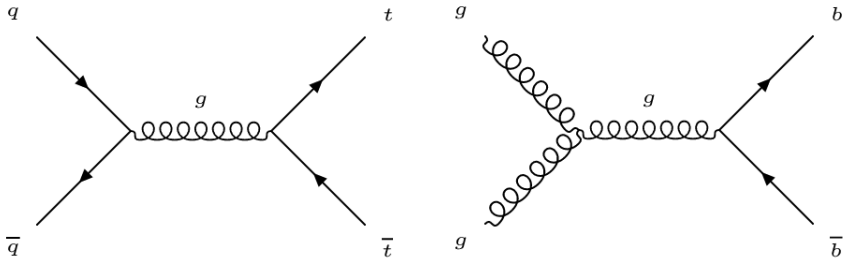

Figure 4.2: Feynman diagrams for the background processes: $t\bar{t}$ on the left and QCD on the right.

4.1 Physics objects reconstruction and identification

All physics objects are reconstructed through the Particle Flow (PF) algorithm [35, 36], which identifies the stable particles produced in the collision combining the information coming from the CMS sub-detectors system, and providing the respective 4-momenta. The list of information is then used to build jets, which preserve part of the information of quarks and gluons in the

hard scattering from which they stem, to determine the missing transverse energy, which gives an estimate of the direction and energy of the neutrinos and other invisible particles. Additionally, it allows to reconstruct and identify taus from their decay products, to quantify charged lepton isolation with respect to other particles, to tag jets coming from the hadronisation of b quarks or top quarks, and, to a minor extent, c quarks or gluons.
First of all, the vertices are reconstructed by a best fit to the intersection of tracks in the tracking system and are defined as good if there are more than four degrees of freedom in the fit and less then 2 cm away in the x-y plane and less than 24 cm away in the z direction from the interaction point: the primary vertex is the vertex corresponding to the highest value of the sum of the squared transverse momentum of all the tracks associated with it. Then the PF candidates are reconstructed, more specifically an iterative tracking algorithm links all the reconstructed elements identifying blocks of elements that are compatible:

- muons are, at first, reconstructed from the hits in the tracking system and then from the track in the muon system. If such particle is identified, the corresponding tracks are removed from the block. The momentum of muons is obtained from the curvature of the corresponding track. The reconstructed track in the muon chamber is named *stand-alone muon*.

- electrons are identified if a charged particle track and one or more ECAL clusters are compatible. After the identification, the tracks are removed from the list. The energy of electrons is determined from a combination of the electron momentum at the primary interaction vertex, the energy of the corresponding ECAL cluster and the energy sum of all bremsstrahlung photons spatially compatible with originating from the electron track.

- charged hadrons are reconstructed from the remaining tracks which can be linked to ECAL and HCAL clusters. The energy is determined from a combination of their momentum measured in the tracker and the matching ECAL and HCAL energy deposits, corrected for the response function of the calorimeters to hadronic showers.

- neutral hadrons are reconstructed from unmatched clusters in HCAL. The energy is obtained from the corresponding corrected ECAL and HCAL energy.

- photons are identified if there are clusters in the ECAL that are not compatible with charged tracks. Their energy is directly obtained from the ECAL measurement.

When the list of PF candidates (photons, electrons, muons, charged and neutral hadrons) is complete, PF jets can be reconstructed offline using

the anti-k_T (AK) jet clustering algorithm[37]. This algorithm clusters the reconstructed PF candidates in each event to form jets based on the angular distance between them and their p_T, after applying the Charged Hadron Subraction (CHS, a correction used to remove the energetic contribution coming from the pile-up interaction) on the group of hardest particles.
The distance between the particle i and the particle j, d_{ij}, and the one between the particle i and the beam, d_{iB}, can be written as follows:

$$d_{ij} = min\left(\frac{1}{p_{T,i}^2}, \frac{1}{p_{T,j}^2}\right)\frac{(\Delta R)_{ij}^2}{R^2}$$

$$d_{iB} = \frac{1}{p_{T,i}^2}$$

with

$$(\Delta R)_{ij}^2 = (\eta_i - \eta_j)^2 + (\phi_i - \phi_j)^2$$

where R is the radius parameter used to define the portion of solid angle covered by the jet, $\eta_{i(j)}$ is the pseudorapidity of the particle $i(j)$ and $\phi_{i(j)}$ is the angle in the transverse plane of the particle $i(j)$.
Jets with $R = 0.4$ are named AK4 or *narrow jets*, while jets with $R = 0.8$ are defined as AK8 or *fat jets*: in this analysis, the latter are considered for the selection of boosted top quark candidates while the first are used to select the b-jets produced by W'.
Jets in both collections have multi-level Jet Energy Corrections (JEC): the jet energy is scaled by a factor that describes the detector response depending on the transverse energy and the pseudorapidity of the jet; to reduce contamination from pile-up events, charged particle candidates not associated to the main primary vertex are subtracted event by event; the energy of the jet is then corrected by the amount of energy deposited by neutral pile-up hadrons in the jet area.

The final state addressed by this analysis is characterised by only jets, therefore, to identify the signal, it will be important to veto the presence of leptons and know how to identify the jets[38].

4.1.1 Electrons

Electron candidates are selected using the selection criteria defined in CMS: different requirements, based on the quality of the track reconstruction and on the matching between the track and the calorimetric cluster, are applied in the barrel and endcaps.
One of the variables used for identification of electrons is the relative isolation, I_{rel}^e, defined as:

$$I_{rel}^e = \frac{I^{ch-h} + max[(I^{\gamma} + I^{n-h} - \rho \times A), 0]}{p_T} \tag{4.1}$$

where p_T is the transverse momentum of electron, ρ is the average energy density not clustered in jets, measured event-by-event, by the cone area A and I^{ch-h}, I^{n-h} and I^{γ} are, respectively, the scalar transverse momentum sums of the charged hadrons, neutral hadrons and photons. The sums are computed in a cone of $\Delta R = 0.3$ around the electron direction .
To veto events with electrons, *veto electrons* are used, for which the average efficiency of selection is $\sim 95\%$ and $I^e_{rel} < 0.198 + 0.506/p_T$ in the barrel and $I^e_{rel} < 0.203 + 0.963/p_T$ in the endcups.

4.1.2 Muons

To veto events with muons, *loose muons* are used.
A loose muon is a particle identified as muon by the Particle Flow algorithm and is reconstructed either as a *global muon* or as a *tracker muon*.
The global muon reconstruction is obtained when a stand-alone muon track is matched with a tracker track, in order to reject the background of muons coming from hadronisation and from the particles that interact around the beam pipe. This approach is especially useful at large transverse momenta because it improves the momentum resolution.
The tracker muon reconstruction is obtained when an algorithm starts from a tracker track and looks for compatible segments in the muon chambers, also considering the energy losses due to the Coulomb scattering. This method is efficient at low momentum (p < 5 GeV), because it requires only a hit in one of the components of the muon chambers.
The I^{μ}_{rel} variable in the muon case, is defined as:

$$I^{\mu}_{rel} = \frac{I^{ch-h} + max[(I^{\gamma} + I^{n-h} - 0.5 \times I^{UP}), 0]}{p_T} \tag{4.2}$$

where I_{PU} is the scalar transverse momentum sum of charged hadrons associated with pile-up vertices. The sums are computed in a cone of $\Delta R = 0.4$ around the muon direction.
For loose muons the average efficiency of selection is $\sim 98\%$ and $I^{\mu}_{rel} < 0.25$.

4.1.3 b-jet identification

Several algorithms for identification of jets originating from b quarks are available in CMS, one of these is the Combined Secondary Vertex version 2 (CSVv2) algorithm[39, 40], which combines discriminating variables for identify a secondary jet, as secondary vertex, number of traces from secondary vertex and track based lifetime, and provides a continuous variable, which will be called cvs, on which more or less strong cuts can be applied.
The long lived particles, as B hadrons, travel a considerable distance from the primary vertex before decaying. The variable used to define the distance between the two vertices is the Impact Parameter (IP), Figure 4.3, that is

a Lorentz invariant.

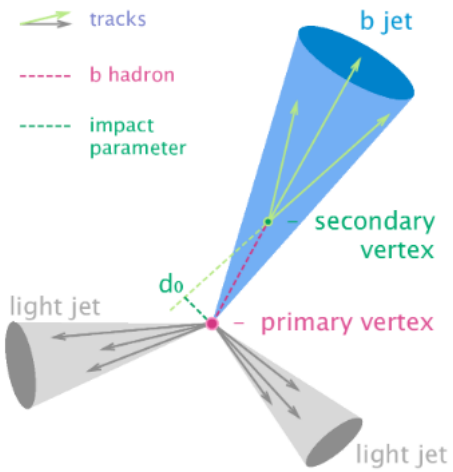

Figure 4.3: Impact Parameter (IP).

4.1.4 top-jet identification

The high boost of the top quark from a W' boson decay causes the three jets to merge into one large jet with a distinct substructure. There are different techniques applied by CMS to tag such jets, the one used in the following, the CMS top-tagging algorithm[41], discriminates the signal jets, according to the jet top-tagging working point corresponding to 3% of mis-tagging rate and based on CHS inputs, using these three variables: jet mass, N-subjettiness and subjet b-tagging.
The jet mass is calculated using the *pruning procedure*[42]. Given the list of constituents in a jet, a recombination algorithm, such Cambridge-Aachen[43] or k_T algorithms, reruns on jets checking for the following condition in each recombination i,j$\longrightarrow$k:

$$\frac{min(p_{T_i}, p_{T_j})}{p_{T_k}} < z_{cut} \qquad \Delta R_{ij} > D_{cut} = \frac{m_{jet}}{p_{Tjet}}, \tag{4.3}$$

where p_T are the magnitude of the transverse momenta of the two subjet candidates and ΔR_{ij} is the distance between candidates. If the conditions are met, the two braches (i and j) are not merged into k and the softer branch is discarded. The algorithm runs the entire list and, at the end, the resulting jet is the pruned jet.
For this analysis, we use $z_{cut} = 0.15$ and $D_{cut} = 0.5$.

The N-subjettiness algorithm[44, 45] defines τ_N variables, which describe the consistency between the jet energy and the number of assumed subjets, N:

$$\tau_N = \frac{1}{d} \sum_i p_{T_i} min(\Delta R_{1,i}, \Delta R_{2,i}, ..., \Delta R_{N,i}),$$

where $\Delta R_{J,i}$ is the distance between the axis of the subjet candidate J and a specific constituent particle i, and d is the normalization factor,

$$d = \sum_i p_{T_i} R,$$

where R is the characteristic distance parameter used by the jet clustering algorithm.
A key step is to choose the candidate subjet directions determined by using geometric measures and requiring the minimization of τ_N: in this case, τ_N is a strictly decreasing function of N, and $0 < \tau_N/\tau_{N1} < 1$.
A jet with a low τ_N value will have energy deposited close to the axes of the N subjet candidates, which is a characteristic of a jet containing N subjets. A top-jet is more consistent with three subjets than two, while a jet from a gluon or light quark will typically be consistent with either two or three subjets. Therefore, the ratio of τ_3 and τ_2 is characteristically smaller for top-jets than for the multijet background and allows to distinguish signal from QCD background.
Finally, we apply the CSVv2 b-tagging algorithm to all of the subjets of the candidate jet found by the top-tagging algorithm.

4.1.5 Reconstruction of W' mass

Once the jets produced by the decay of the W' boson have been identified, and of these obtained energy and transverse momentum, it is possible to get the invariant mass of W':

$$M_{W'} = \sqrt{\left(\sum_i E_i\right)^2 - \left(\sum_i \vec{p}_i\right)^2} \tag{4.4}$$

with

$$\begin{aligned} p_x &= p_T \ cos\phi \\ p_y &= p_T \ sen\phi \\ p_z &= p_T \ senh \ \eta \\ |\vec{p}| &= p_T \ cosh \ \eta \end{aligned} \tag{4.5}$$

Chapter 5

Analysis strategy

This chapter describes the analysis strategy to extract the W' signal.
At first, a series of topological and kinematic selection requirements are applied in order to discriminate the signal from the background and to identify the signal region. Then, reversing some of those criteria, control regions are identified to extract the main backgrounds, i.e. the $t\bar{t}$ pair production and QCD multijet events, directly from data, with a so-called *Data-Driven* method. A maximum likelihood fit on the invariant mass of reconstructed W' candidates is performed in the signal region, for different hypothesis made on the W' boson mass, into range 1000-4000 GeV. In absence of signal evidence, upper limits are derived on the W' production cross section.

5.1 Data and simulated samples

The list of data sets employed in this analysis is reported in Table 5.1: the label JetHT refers to the set of triggers used to select the data set based on the properties of jets and hadronic energy reconstructed in the events at trigger-level, the label Run2016B through H3 refers to the data taking period, the label 03Feb2017 refers to the date in which the data sets have been processed, the final label MINIAOD refers to the file format and content according to CMS standard definitions.
The data set used corresponds to an integrated luminosity of 35.872 fb^{-1} known with a relative uncertainty of 2.6%.

Signal and the main background processes are taken from simulation of events at the LHC, obtained by event generators based on MC methods.
The signal event samples are generated with the *CompHEP* event generator[46] with different benchmark models based on the hypothesis made on the W' boson mass, ranging from 1000 up to 4000 GeV in steps of 200 GeV, considering the W' boson right-handed and with the width of the resonance mass of 1%.

Data set	Integrated luminosity $[pb^{-1}]$
/JetHT/Run2016B-03Feb2017_ver2-v2/MINIAOD	5790±150
/JetHT/Run2016C-03Feb2017-v1/MINIAOD	2570±70
/JetHT/Run2016D-03Feb2017-v1/MINIAOD	4250±110
/JetHT/Run2016E-03Feb2017-v1/MINIAOD	4010±100
/JetHT/Run2016F-03Feb2017-v1/MINIAOD	3100±80
/JetHT/Run2016G-03Feb2017-v1/MINIAOD	7500±200
/JetHT/Run2016H2-03Feb2017_ver2-v1/MINIAOD	8400±200
/JetHT/Run2016H3-03Feb2017_ver3-v1/MINIAOD	221±6

Table 5.1: List of data sets of proton-proton collision data produced at $\sqrt{s}$= 13 TeV and collected by CMS in 2016, employed in the thesis. Data collected correspond to an integrated luminosity of 35.872 fb^{-1} known with a relative uncertainty of 2.6%.

CompHEP is used for the leading order (LO) cross section calculation, which is then scaled to next-to-leading order (NLO) using a factor of 1.2[47]. The generated signal samples for the W' process and the corresponding theory cross sections are reported in Table 5.2.

Mass [GeV]	Cross section $[pb]$
1000	$2.6^{+0.2}_{-0.3}$
1200	$1.24^{+0.09}_{-0.11}$
1400	$0.64^{+0.06}_{-0.07}$
1600	$0.35^{+0.03}_{-0.04}$
1800	$0.20^{+0.02}_{-0.02}$
2000	0.115±0.014
2200	0.069±0.001
2400	$0.042^{+0.007}_{-0.006}$
2600	0.026±0.004
2800	$0.021^{+0.004}_{-0.003}$
3000	$0.0108^{+0.0019}_{-0.0017}$
3200	$0.0070^{+0.0012}_{-0.0011}$
3400	$0.0046^{+0.0007}_{-0.0006}$
3600	$0.0031^{+0.0005}_{-0.0004}$
3800	$0.0021^{+0.0005}_{-0.0004}$
4000	$0.0014^{+0.0003}_{-0.0002}$

Table 5.2: Simulated $W' \longrightarrow tb$ samples employed in the analysis with their corresponding production cross sections (LO).

The $t\bar{t}$ pair production process is generated with *Powheg 2.0*[48], and its cross section is calculated at the next-to-next-to leading order (NNLO) in perturbative QCD. Two additional simulated samples are generated to increase the $t\bar{t}$ process statistics in the signal region, by generating events where the mass of the $t\bar{t}$ pair is greater 700 GeV, and the corresponding cross sections are evaluated at next-to leading order.

QCD multijet processes are generated with *MadGraph 5*[49] and their cross sections are calculated at leading order.
The simulated samples for background processes used in this thesis and the corresponding theory cross sections[50] are reported in Table 5.3.

Sample	Cross section [*pb*]
$t\bar{t}$ (0-700)	830^{+20}_{-30}
$t\bar{t}$ (700-1000)	$80.5^{+1.6}_{-3.0}$
$t\bar{t}$ (1000-Inf)	$21.3^{+0.4}_{-0.9}$
QCD (300-500)	347700±80
QCD (500-700)	32100±7
QCD (700-1000)	6831.0±1.7
QCD (1000-1500)	1207.9±0.5
QCD (1500-2000)	119.90±0.06
QCD (2000-Inf)	25.24±0.02

Table 5.3: Simulated samples for background processes used in the analysis with their corresponding production cross sections. The samples are split in order to increase the available statistics by generating additional events in more extreme regions of the phase space. The $t\bar{t}$ sample is divided considering different ranges of $t\bar{t}$ pair mass, instead QCD sample is split taking in account different values of the total transverse momenta.
The $t\bar{t}$ (0-700) cross section is an inclusive cross section, then it is corrected in order by removing the contribution from the samples at higher $t\bar{t}$ mass.

CompHEP, Powheg and Madgraph5 generate matrix elements of hard scattering process at leading order corrections, for the first two, and at next-to-leading order corrections for the latter.
Pythia 8[51] generates and simulates the parton-shower of quarks produced in proton-proton collisions that hadronize.
The simulation of stable particles interactions with CMS sub-detectors is performed using *Geant4* [52].

All simulated event samples include additional interactions with respect to the primary one (pile-up) that are weighted such that the distribution in the number of interactions agrees with that expected in data. This procedure, also called "reweighting", consists in applying multiplicative factors to simulated sample events to correct for the discrepancy with the distribution of primary vertices in the data.

5.2 Event selection

In order to discriminate the signal from the background, a series of topological and kinematic selection requirements, or "cuts", are applied, taking into account that the final state considered is fully hadronic, consisting of products of hadronisation of the b quark and the top quark decaying through the t$\longrightarrow$Wb$\longrightarrow$qq'b chain. In particular, final states are considered where an Anti-Kt jet with radius parameter 0.8, AK8, described in the chapter 4, is produced by the boosted top quark, and an additional AK jet with radius parameter 0.4 produced by the b quark.

The trigger for this analysis requires that the linear sum of the energy in the transverse plane of jet is greater than 800 GeV. Furthermore the events are selected with at least one AK4 jet and at least one AK8 jet and by vetoing loose muons and veto electrons, as defined in section 4.1. Moreover, at least one AK8 jet is identified as top-jet and at least one AK4 jet is identified as a b-tagged jet, in tight working point according to the CSV discriminator, which corresponds to a value of the discriminator greater than 0.9535.
The hadronic decay products of a top quark are produced highly collimated because of the Lorentz boost of the top quark, so they can be reconstructed in a single large-radius jet, or top-jet. This top-jet is defined by requesting that the jet invariant mass lies between 150 GeV and 220 GeV, its transverse momentum is greater than 400 GeV, the ratio between τ_3 and τ_2 is less than 0.55 (tight working point) and at least one subjet is b-tagged in medium working point (csv>0.8484).
The b-jets in the signal region are selected only if they don't overlap with the top quark, by using an angular separation criteria which requires ΔR >1.2. To reduce the contamination from $t\bar{t}$ events in the signal region, a further cut is applied that allows to exclude events where the b-jet is identified as part of a larger-radius top jet that does satisfy looser selection criteria, meaning has a mass between 150 GeV and 220 GeV and no reconstructed subjet. Events where the b-jet is instead matched with such a candidate are defined as "matched events".

This set of requirements is summarized here:

- **trigger**:
  - HT > 800 GeV;
- **pre-selection**:
  - veto on loose muons;
  - veto on veto electrons;
  - at least one AK4 jet;
  - at lest one AK8 jet;

- **identification AK8 jet**:
  - 150 GeV $< m <$ 220 GeV;
  - $p_T >$ 400 GeV;
  - $\tau_3/\tau_2 < 0.55$ (tight working point);
  - csv>0.8484 (medium working point);

- **b-tagged AK4 jet**:
  - $\Delta R = \sqrt{\Delta\phi^2 + \Delta\eta^2} = \sqrt{(\phi_{top\ jet} - \phi_{AK4})^2 + (\eta_{top\ jet} - \eta_{AK4})^2} > 1.2$;
  - csv>0.9535 (tight working point);

- **b-tagged AK4 jets matched to a loose top quark candidate**:
  - csv_{AK4} >0.9535 (tight working point);
  - $\Delta R = \sqrt{\Delta\phi^2 + \Delta\eta^2} = \sqrt{(\phi_{AK8} - \phi_{AK4})^2 + (\eta_{AK8} - \eta_{AK4})^2} < 1.2$;
  - 150 GeV $< m_{AK8} <$ 220 GeV;

and identifies the signal region (SR), that is the region of phase space enriched in signal events.
The Table 5.4 shows the number of events normalized to the cross section that exceed all the cuts which identify the SR for each simulated sample used for the analysis, and the selection efficiency for the same samples.

Background sample	Number of events	Efficiency
$t\bar{t}$	2330±20	$0.0005979817 \pm 2 \cdot 10^{-10}$
QCD	5700±300	$0.00000947600 \pm 2 \cdot 10^{-11}$
Signal sample	Number of events	Efficiency
W' (1000)	613±18	$0.0119400 \pm 5 \cdot 10^{-7}$
W' (1200)	707±13	$0.0168136 \pm 6 \cdot 10^{-7}$
W' (1400)	370±7	$0.0166933 \pm 6 \cdot 10^{-7}$
W' (1600)	189±4	$0.0154650 \pm 6 \cdot 10^{-7}$
W' (1800)	90±2	$0.0129444 \pm 6 \cdot 10^{-7}$
W' (2000)	43±1	$0.0106850 \pm 1.5 \cdot 10^{-6}$
W' (2200)	21.6±0.5	$0.0089700 \pm 5 \cdot 10^{-7}$
W' (2400)	11.9±0.3	$0.0079044 \pm 5 \cdot 10^{-7}$
W' (2600)	5.97±0.18	$0.0066422 \pm 4 \cdot 10^{-7}$
W' (2800)	4.23±0.13	$0.0057179 \pm 4 \cdot 10^{-7}$
W' (3000)	2.00±0.06	$0.0052750 \pm 4 \cdot 10^{-7}$
W' (3200)	1.20±0.04	$0.0049399 \pm 4 \cdot 10^{-7}$
W' (3400)	0.71±0.03	$0.0045400 \pm 3 \cdot 10^{-7}$
W' (3600)	0.47±0.02	$0.0044450 \pm 3 \cdot 10^{-7}$
W' (3800)	0.30±0.01	$0.0042500 \pm 3 \cdot 10^{-7}$
W' (4000)	0.197±0.007	$0.0041250 \pm 3 \cdot 10^{-7}$

Table 5.4: Number of events normalized to the cross section that exceed all cuts which identify the SR for each simulated sample used for the analysis, and the selection efficiency for the same samples.

Below are the distributions of the variables on which the cuts are applied, before the selection is applied:

- number of loose muons, number of veto electrons, number of AK8 jets and number of AK4 jets after the trigger selection, in Figure 5.1;
- ratio between τ_3 and τ_2, AK8 jet mass and AK8 jet transverse momentum after the pre-selection, in Figure 5.2;
- ΔR, csv, number of AK8 jets and number of AK4 jets after the AK8 jet identification, in Figure 5.3.

Moreover, it is interesting to observe how $M_{W'}$ distribution changes with and without the cut on the matched events. In Figure 5.4, it is possible to observe the distribution before the veto on the matched events, after having applied the cut and the distribution for the only matched events.

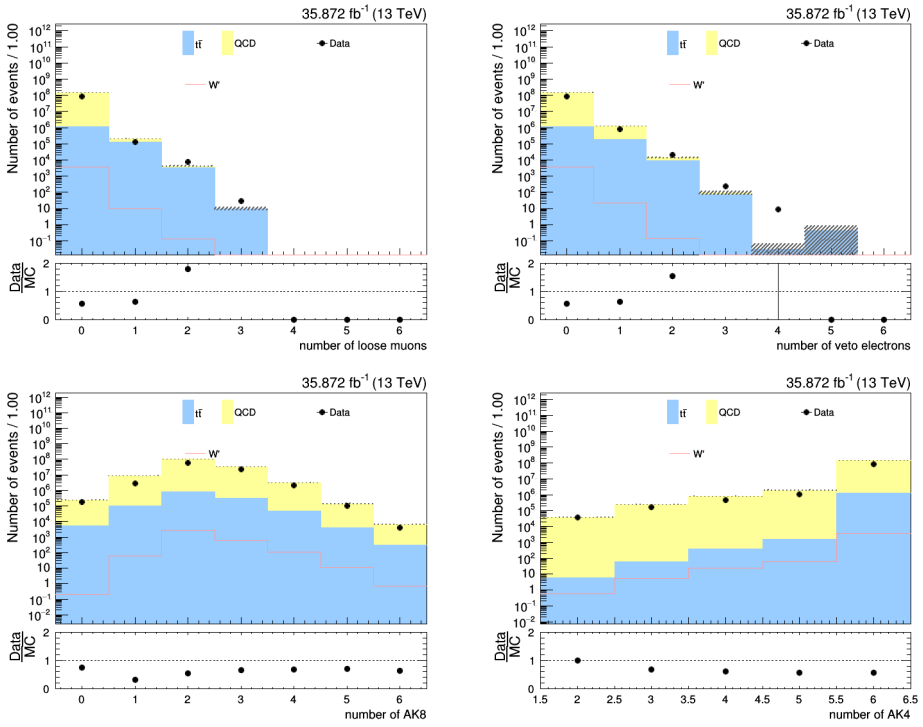

Figure 5.1: Distribution of number of loose muons (top-left), number of veto electrons (top-right), number of AK8 jets (bottom-left) and number of AK4 jets (bottom-right) after the trigger selection.
Note that the range for the distribution of number of AK4 jet starts at 2, and not 0, because of the selection criteria used for generating simulated samples.

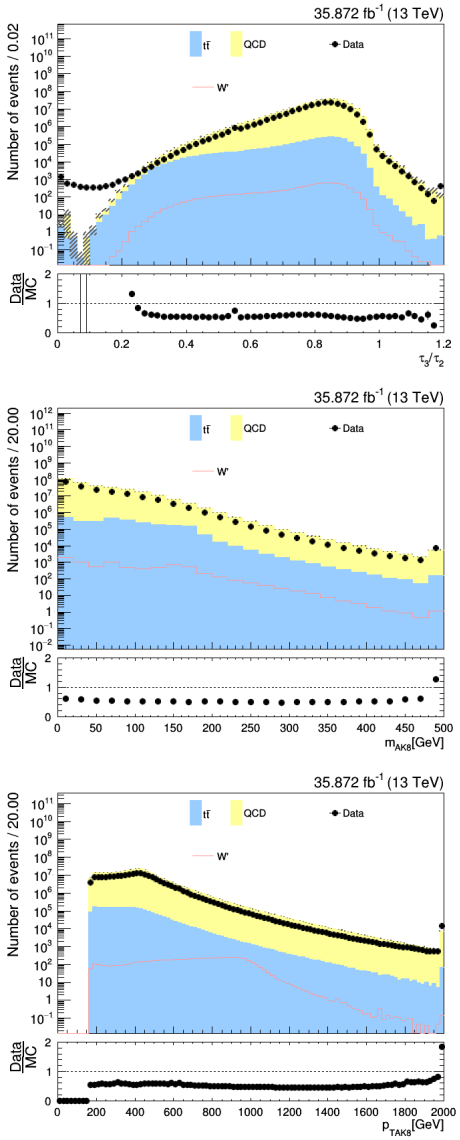

Figure 5.2: Distribution of ratio between τ_3 and τ_2 (top), AK8 jet mass (center) and AK8 jet transverse momentum (bottom) after the pre-selection.

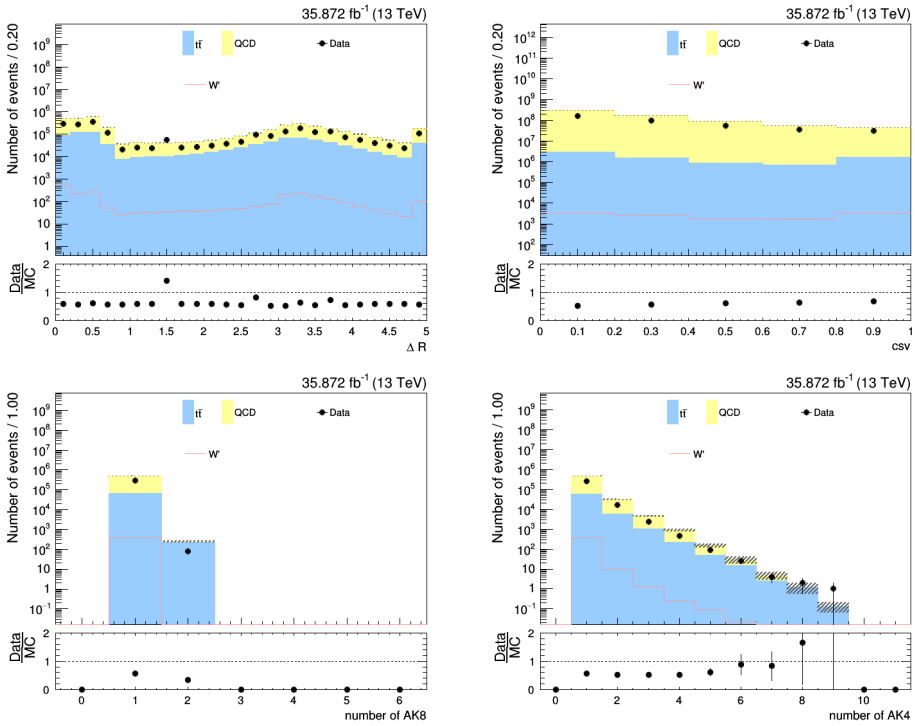

Figure 5.3: Distribution of ΔR (top-left), csv (top-right), number of AK8 jets (bottom-left) and number of AK4 jets (bottom-right) after the AK8 jet identification.

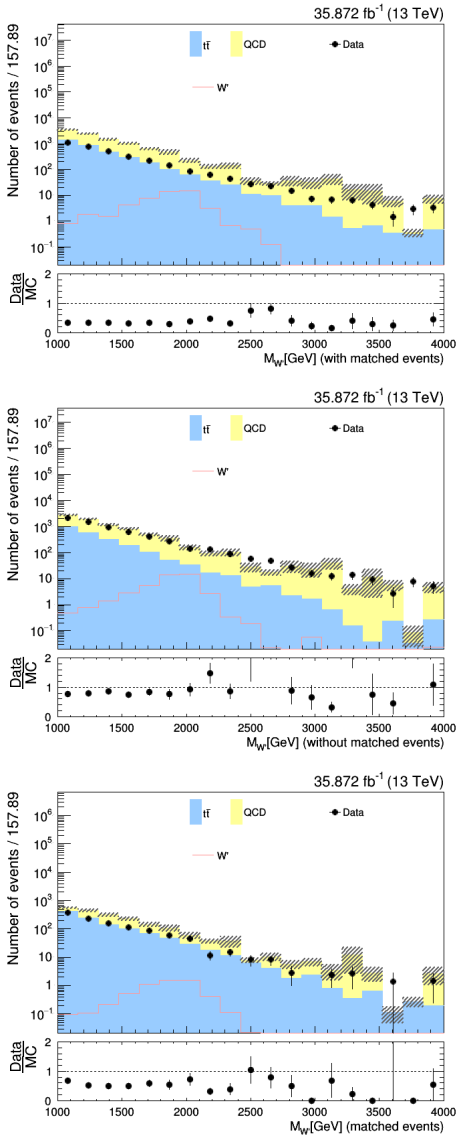

Figure 5.4: $M_{W'}$ distribution before the veto on the matched events (top), after having applied the cut (center) and the distribution for the only matched events (bottom).

In Table 5.5, instead, the selection efficiency for the cut on the matched events, in the SR, for the simulated samples is reported.

Sample	Efficiency
W'	89.5±0.6 %
$t\bar{t}$	67.750±0.014 %
QCD	86.740±0.005 %

Table 5.5: Selection efficiency for the cut on the matched events, in the SR, for the simulated samples.

In order to perform the signal extraction, four regions (CR) are introduced, labeled A, B, C, and D, by making use of two variables: the number of b-tagged AK4 jets and the ratio τ_3/τ_2. The totality of the four regions is also henceforth referred to as region ABCD for brevity.
As shown in the Figure 5.5:

- if the number of b-tagged AK4 jets is equal to 1 and the ratio τ_3/τ_2 is less than 0.55, the event is assigned to region A (or signal region, SR);
- if the number of b-tagged AK4 jets is equal to 0 and the ratio τ_3/τ_2 is less than 0.55, the event is assigned to region B (a control region, CR);
- if the number of b-tagged AK4 jets is equal to 1 and the ratio τ_3/τ_2 is greater than 0.55, the event is assigned to region C (a control region, CR);
- if the number of b-tagged AK4 jets is equal to 0 and the ratio τ_3/τ_2 is greater than 0.55, the event is assigned to region D (a control region, CR).

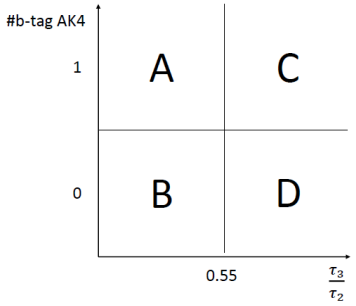

Figure 5.5: Region ABCD defined by two variables: the number of b-tagged AK4 jets (#b-tag AK4) and the ratio τ_3/τ_2.

5.3 Background estimation

Since the study of QCD processes is not at all simple and there are large limits on the predictive capacity of simulation at leading order in our region of the phase space, in this analysis we do not solely rely on the simulation, but we estimate the shape and yield of background from data thanks to a Data-Driven method (DD). In order to accomplish this, and to validate the method, a further set of control regions (region XYZT) is introduced to cross-check the method. The region XYZT is obtained in a similar way to the region ABCD, the only difference being the cut on the subjet of the AK8 jet which is considered not b-tagged in this region.

By comparing the simulated background in region A with those in region X, as shown in Figure 5.6, it is possible to note that $t\bar{t}$ processes in region A are not negligible compared to QCD multijet processes, unlike in the region X; therefore, the DD method is applied in the X region considering the whole background as if it were only QCD processes and then a new systematic uncertainty is introduced to check the $t\bar{t}$ effects on QCD shape extraction.

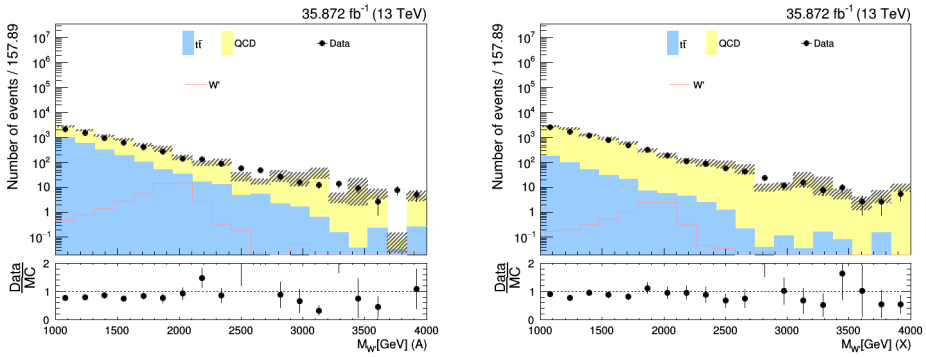

Figure 5.6: $M_{W'}$ distribution for simulated samples in region A (left) and in region X (right).

In region XYZT, we expect the shape of $M_{W'}$ distribution for background in the region Z to be similar to the one in the region X, modulo a function that we want to extract from data itself. This function is a bin-by-bin transfer function (TF) defined by taking the ratio of the $M_{W'}$ distributions in the regions Y and T. So, for each bin:

$$M_{(W',X)} := M_{(W',Z)} \frac{M_{(W',Y)}}{M_{(W',T)}} = M_{(W',Z)}\ TF = M_{(W',ZY/T)}\ .$$

The $M_{W'}$ distribution in the region X, Y, Z and T, is shown in Figure 5.7, while the TF distribution and the comparison between $M_{(W',X)}$ distribution and $M_{(W',ZY/T)}$ distribution are in Figure 5.8.

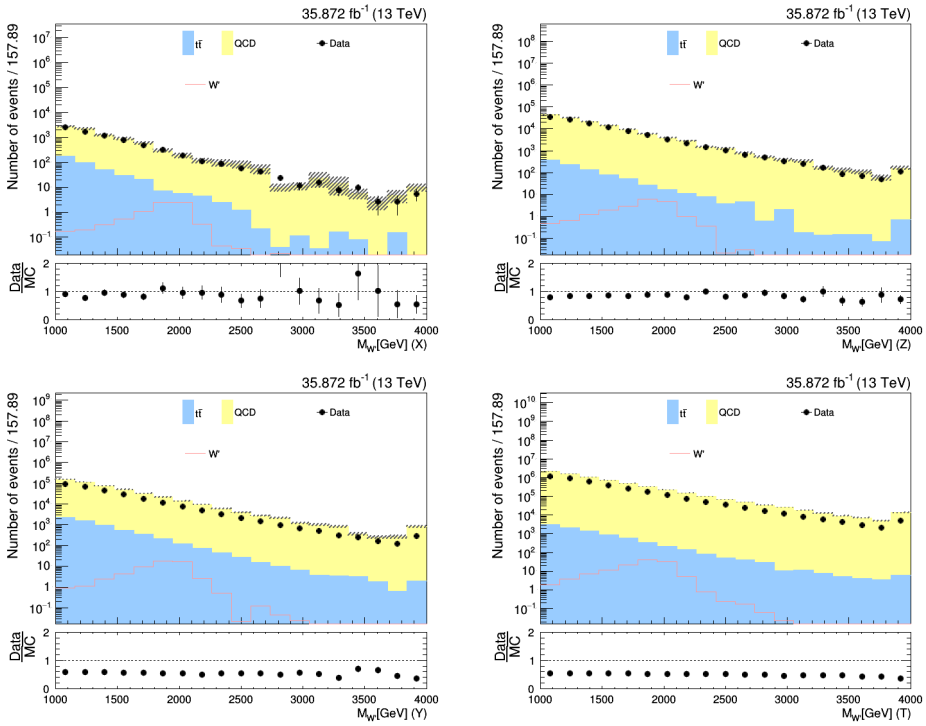

Figure 5.7: $M_{W'}$ distribution in the region X (top-left), Y (bottom-left), Z (top-right) and T (bottom-right).

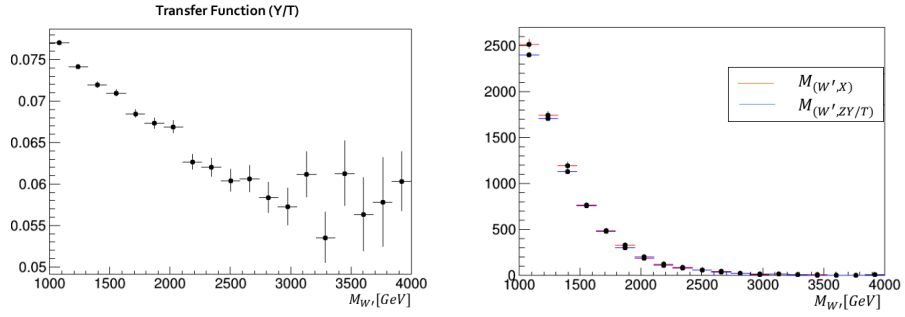

Figure 5.8: TF distribution (left) and the comparison between $M_{(W',X)}$ distribution and $M_{(W',ZY/T)}$ distribution (right) in region XYZT.

Furthermore, the distribution is normalized by a scale factor (SF_{MC}) obtained from simulated QCD events, in order to correct between the residual differences across the regions, to take into account in particular the bias in the extrapolation of the ratio from the regions Y,T to Z,X.
This factor is obtained by evaluating the ratio between the yields in the Y/T region and in the X/Z region, and using them in the following way:

$$SF_{MC} = \frac{I(M_{W',X})}{I(M_{W',Z})} / \frac{I(M_{W',Y})}{I(M_{W',T})} = \frac{I(M_{W',X})I(M_{W',T})}{I(M_{W',Y})I(M_{W',Z})}.$$

Figure 5.9 compares the $M_{W'}$ distribution in region X with simulated background to the one with DD background (BKG-DD): the latter presents a better adaptation to data; part of this is due to the fact that the statistics available in simulation is limited, and part to the improvement due to the extraction itself.
The residual disagreement will be taken into account with the addition of systematic uncertainties described later on.

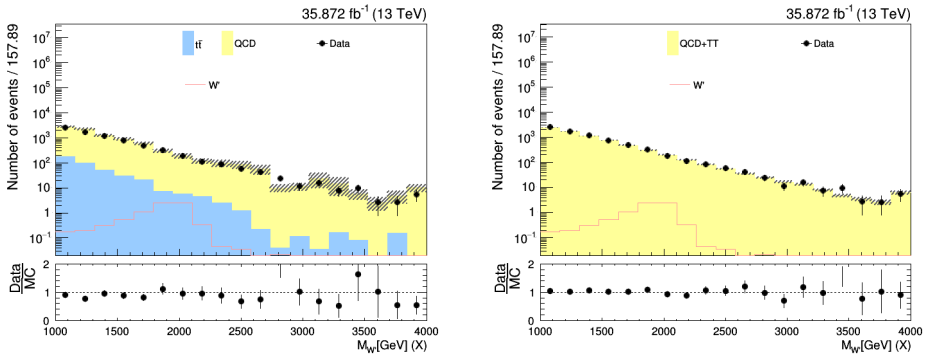

Figure 5.9: $M_{W'}$ distribution with simulated background (left) and $M_{W'}$ distribution with DD background (right) in region X.

The same procedure can be applied in the region ABCD.
The $M_{W'}$ distribution in the region A, B, C and D, is shown in Figure 5.10, while the TF distribution and the comparison between $M_{(W',A)}$ distribution and $M_{(W',CB/D)}$ distribution are shown in Figure 5.11.
By applying the DD method, the result of Figure 5.12 is obtained.

By comparing the $M_{W'}$ distribution in the region X (A) with the one obtained with the DD method applied in the region XYZT (ABCD), as shown in Figure 5.8 (Figure 5.11), the two distributions have discrepancies, so a new systematic uncertainty, henceforth labeled "qcd-DD", is introduced to take into account these differences.
Uncertainties on the different behavior of $t\bar{t}$ and QCD multijet backgrounds are also considered.

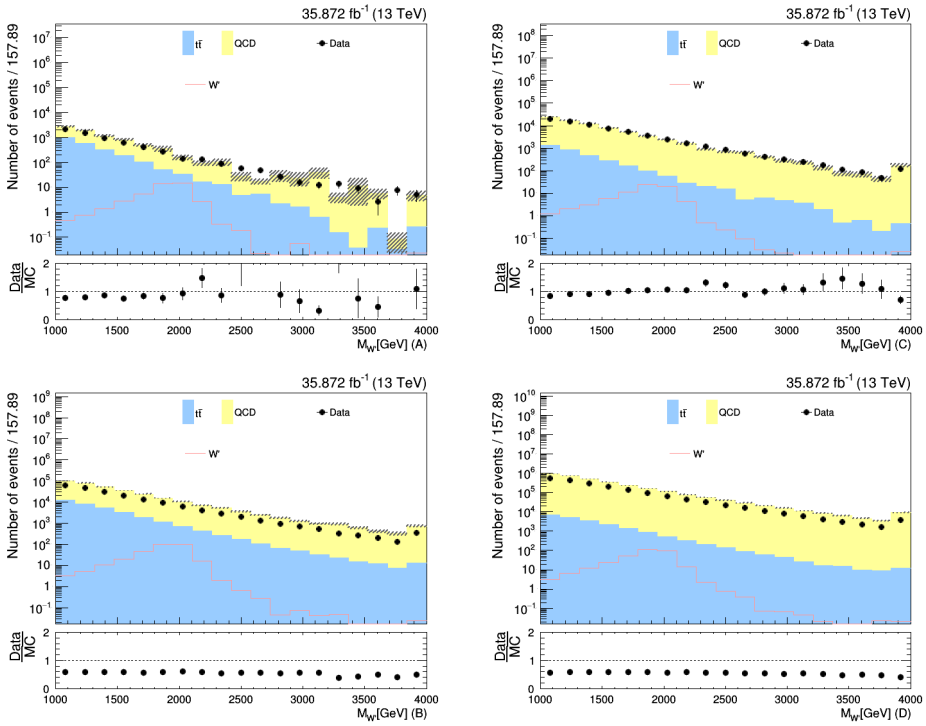

Figure 5.10: $M_{W'}$ distribution in the region A (top-left), B (bottom-left), C (top-right) and D (bottom-right).

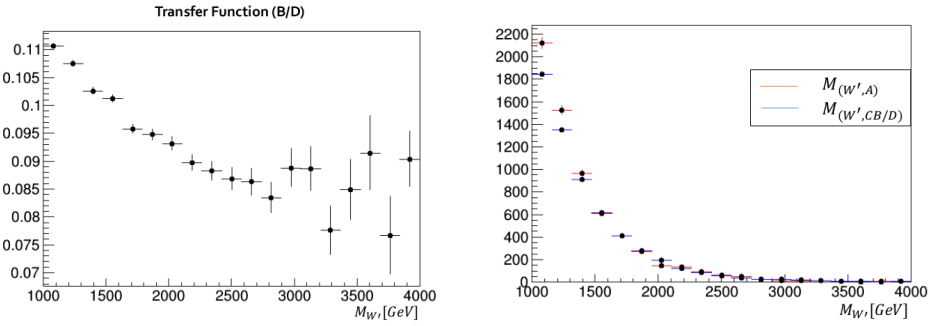

Figure 5.11: TF distribution (left) and the comparison between $M_{(W',A)}$ distribution and $M_{(W',CB/D)}$ distribution (right) in region ABCD.

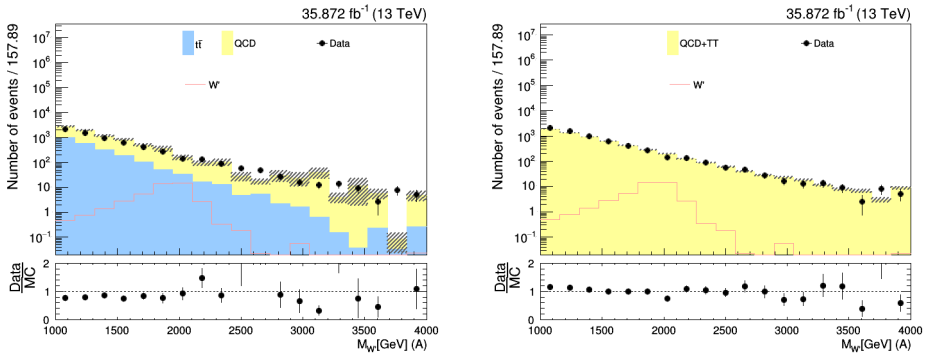

Figure 5.12: $M_{W'}$ distribution with simulated background (left) and $M_{W'}$ distribution with DD background (right) in region ABCD.

5.4 Systematics uncertainties

Systematic uncertainties do affect background and signal prediction, and have to be taken into account when extracting the signal value from the fit. The effect of the systematics can be of two types:

- **yield effect only**: those effects modify just the yield of the distribution of the variable used in the fit;
- **yield and shape effect**: they do alter the yield and the shape of the distribution of the variable used in the fit, changing not only in a flat way the distribution but also re-shaping it.

The sources of systematic uncertainties used in this analysis are:

- **luminosity**: the integrated luminosity it is known with a relative uncertainty of 2.6% [53];
- **b-tagging efficiency scale factors**: in order to correct the b-tagging efficiency estimated from control samples in 13 TeV data [54], scale factors have to be applied on simulated events. The errors introduced with the use of scale factors are propagated summing or subtracting the associated uncertainty to the nominal value. The variations from the central value obtained in this way represent the systematic uncertainties for the b-tagging;
- **top-tagging scale factors**: as for the b-tagging efficiency scale factors, in order to correct the efficiency in tagging a boosted fat jet as top quark, scale factors have to be applied on simulated events. The variations from the central value obtained in this way represent the systematic uncertainties for the top quark tagging;

- **factorisation and renormalisation scales**: the uncertainty introduced by variations in the factorisation and renormalisation scales is estimated by using distributions obtained by halving or doubling the scales. The effect is estimated for each process separately, in fact, the uncertainties for the different backgrounds are considered uncorrelated;

- **pile-up modelling**: in order to correct for the number of primary vertices in data and in the simulated samples, a scale factor is applied. The systematic uncertainties related to pile-up modelling are taken into account by varying by ±4.6% the minimum bias cross section used to calculate the data pile-up distributions;

- **QCD modelling**: the distribution of $M_{W'}$ obtained by applying the DD method is not identical to predicted distribution. The scale factors that take into account this difference are defined by variation of the two distributions in the region XYZT with respect to the predicted distribution in the same region, and they are defined, with X′=Z Y/T, as:

$$SF_{up/down} = \pm \frac{M_{(W',X)} - M_{(W',X')}}{M_{(W',X')}}.$$

  The scale factors are applied to BKG-DD, obtaining the distributions in Figure 5.13.

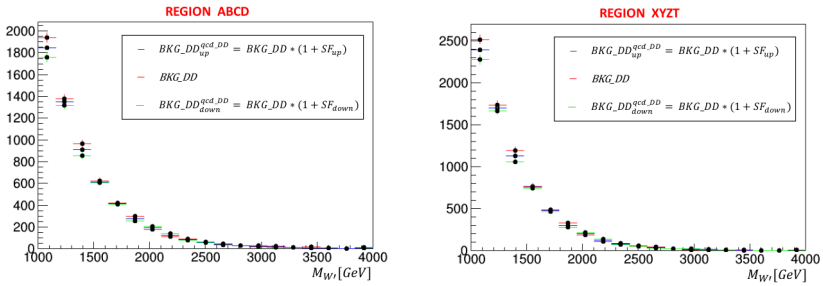

Figure 5.13: $M_{W'}$ distribution for DD background with the "up" and "down" variation for the qcd-DD systematic uncertainty applied in the region ABCD (left) and in the region XYZT (right).

- $t\bar{t}$ **variation**: the $t\bar{t}$ and QCD multijet TF can behave in a different manner, and, to take this into account, an uncertainty on the $t\bar{t}$ contribution is derived from simulation and applied to the DD shape. Such uncertainty allows to alter the shape of the distribution to extract such contamination from data directly. By varying the $t\bar{t}$ contribution in the simulated background by an amount α (BKG = QCD + α $t\bar{t}$), with α equal to 1 for the nominal file, equal to 2 for the "up" variation and equal to 0.5 for the "down" variation , it is possible to take

into account the $t\bar{t}$ effects on QCD shape extraction by introducing the scale factors defined by the ratio of changed transition function (TF_{up} or TF_{down}) and the nominal transition function (TF).
The scale factors are applied to BKG-DD, obtaining the distributions in Figure 5.14.

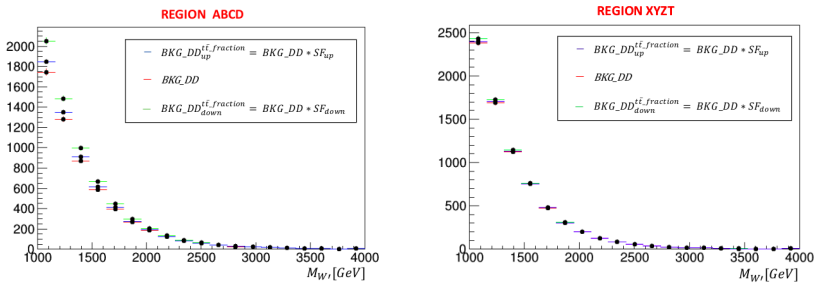

Figure 5.14: $M_{W'}$ distribution for DD background with the "up" and "down" variation for $t\bar{t}$-fraction systematic uncertainty applied in region ABCD (left) and in region XYZT (right).

5.5 Fit procedure and results

Once the cuts for selection of the signal events have been optimized, the background shape has been obtained, and the systematic uncertainties of interest have been reconstructed, it is possible to test the hypothesis of existence of W' boson by using a binned maximum likelihood fit to data in the region A (signal region). The fit is performed for the variable $M_{W'}$, taking into account the background estimated from data thanks to the DD method. Since for the variable used signal distributions depend on the W' mass, the model considered include 16 mass points ranging from 1000 GeV up to 4000 GeV in steps of 200 GeV.

Typically, we want to discriminate between two hypotheses:

- $\mathbf{H}_0$ that assumes the absence of new physics, i.e. the signal is absent or too little to be detected;
- $\mathbf{H}_1$ that assumes the presence of the new W' resonance;

and we indicate with ν the expected number of event, i.e. $\nu = b$ for H_0 hypothesis and $\nu = \mu s + b$ for H_1 hypothesis, where s and b are the expected yields of signal and background, respectively, and μ is the *signal strength*. All possible values of the expected signal yield are obtained by varying μ: $\mu = 1$ corresponding to the theory prediction.

The likelihood [55] associated with the current analysis is the product of a Poissonian distribution, representing the distribution for the number of events of signal and background, multiplied by a second term that represents the signal and background models:

$$\mathcal{L}(obs|\mu,\theta) = Poisson(n, \mu \cdot s(\theta) + b(\theta)) f(x_k|\mu,\theta)$$

where the *signal strength* μ is defined as the ratio of the value of the fitted parameter before and after the fit, θ is the set of systematics uncertainties to be profiled, named nuisance parameters, n is the number of events, $s(\theta)$ and $b(\theta)$ are the expected yields of signal and background depending from the unknown parameters, respectively, while the probability distribution function $f(x_k|\mu,\theta)$ is defined as a combination of two PDFs one for signal f_s and one for background:

$$f(x_k|\mu,\theta) = \frac{\mu \cdot s(\theta)}{\mu \cdot s(\theta) + b(\theta)} f_s(x,\theta) + \frac{b(\theta)}{\mu \cdot s(\theta) + b(\theta)} f_b(x,\theta).$$

A shape analysis for the binned maximum likelihood technique is performed: in this case there are two process, signal and background, and for each independent source of systematic uncertainty, a nuisance parameter is considered.
The background normalization uncertainties are modeled with a coefficient for the background templates with a log-normal prior.
For each shape uncertainty and process affected by it, two shapes are obtained shifting that parameter up and down by one standard deviation. When building the likelihood function, each shape uncertainty is associated to a nuisance parameter taken from a unit Gaussian distribution, which is used to interpolate between the nominal template and other two shifting.

The fit results are returned in term of signal strength μ, and in Table 5.6 are reported the results obtained with the fit to $M_{W'}$ by considering a signal with mass 2000 GeV, using a data driven background and the nuisance parameters of section 5.4: the values found for the central value and uncertainty on nuisance parameters (*pulls*), the ratio of error in the model before and after the fit, and the correlation coefficient ρ between the signal strength μ and each nuisance parameter. With Δx is indicated the difference between the value of the parameter before and after the fit, σ_{in} and σ_{out} are, respectively, the error in the model before and after the fit.
In Figure 5.15 are plotted the same parameters reported in the Table 5.6.
The analysis is repeated for different hypothesis made on the W' boson mass and the result of each fit is shown in the Table 5.7.
Since in the outcomes there is no evidence for a new signal, upper limits are set on the cross section of W' bosons decaying to tb for the benchmark models.

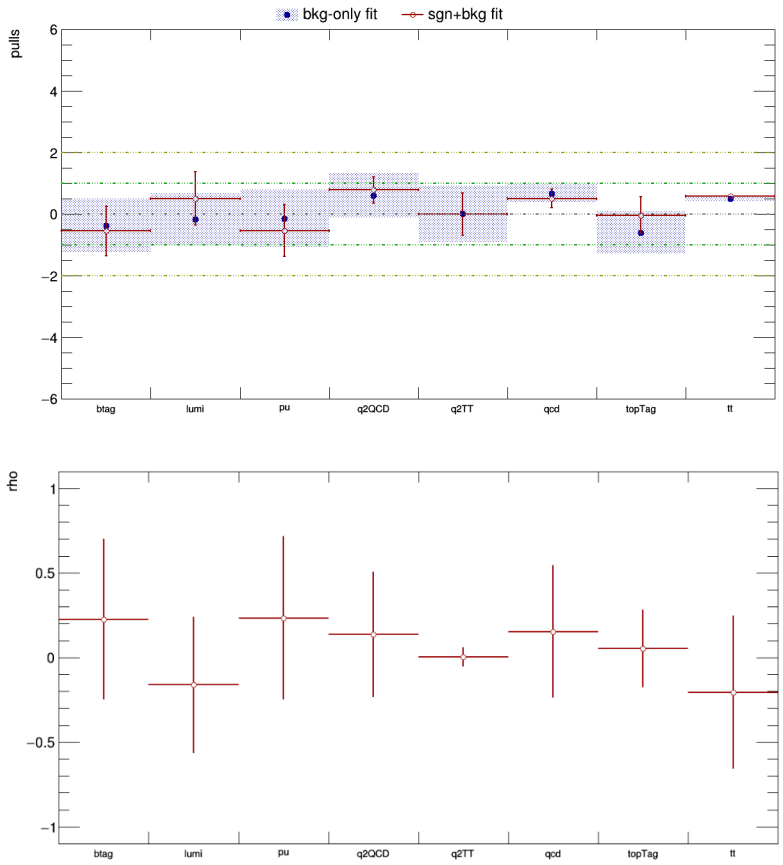

Figure 5.15: Pulls for each nuisance parameter (top) and the correlation coefficient between the signal strength μ and for each nuisance parameter (bottom).

	b-only fit		b+s fit		
Systematic uncertainty	$\Delta x/\sigma_{in}$	σ_{out}/σ_{in}	$\Delta x/\sigma_{in}$	σ_{out}/σ_{in}	$\rho(\theta\mu)$
lumi	-0.17	0.86	+0.50	0.86	-0.1618
btag	-0.38	0.88	-0.55	0.80	+0.2263
topTag	-0.60	0.69	-0.04	0.59	+0.0528
pu	-0.14	0.94	-0.54	0.84	+0.2339
q^2_{QCD}	+0.60	0.73	+0.78	0.43	+0.1377
$q^2_{t\bar{t}}$	+0.01	0.91	0.00	0.69	+0.0033
qcd-DD	+0.67	0.30	+0.50	0.30	+0.1530
$t\bar{t}$-fraction	+0.49	0.08	+0.58	0.08	-0.2055

Table 5.6: Pulls for the main nuisance parameters, the ratio of error in the model before and after the fit and the correlation coefficient ρ between the signal strength μ and each nuisance parameter.

The limits are calculated with a dedicated software, the *Combine tool* [56], in order to quantify the level of incompatibility of data with a signal hypothesis. The expected and observed upper limits are calculated with the modified frequentist method [57, 58, 59], and the systematic uncertainties described in section 5.4, are taken into account as nuisance parameters, affecting both the signal and the background.
The test statistic used for the calculation of the limits is the ratio of the likelihood of the hypothesis H_0 and H_1, and allows to discriminate signal-like events from background-like ones:

$$\lambda = \frac{\mathcal{L}(obs|H_1)}{\mathcal{L}(obs|H_0)}$$

Considering the nuisance parameters of the two hypotheses, a profile likelihood ratio, used as test statistic, is:

$$q_\mu = -2ln\lambda(\mu,\theta) = -2ln\left[e^{-\mu s(\theta)}\prod_{i=1}^{n}\left(\frac{\mu s(\theta) f_s(x_i|\theta)}{b(\theta) f_b(x_i|\theta)} + 1\right)\right].$$

Events with $q_\mu \geq 0$ appear to be under the hypothesis of background only, viceversa for the hypothesis of background plus signal.
In order to quote an upper limit using the frequentist approach, the distribution of the test statistic q_μ in the hypothesis of signal plus background has to known, and the p-value[1] corresponding to the observed value $q_\mu = q_\mu^{obs}$, denoted as p_{s+b}, has to be determined as a function of the parameters of interest μ.

[1] p-value is the probability that considered the test q_μ assumes a value grater or equal to the observed one in the case of pure background fluctuation.

Mass [GeV]	μ
1000	$+0.24\pm0.12$
1200	$+0.31\pm0.15$
1400	-0.24 ± 0.19
1600	-0.7 ± 0.3
1800	$-1.1^{+0.5}_{-0.4}$
2000	-2.2 ± 0.8
2200	$+1.4\pm1.4$
2400	$+4\pm2$
2600	$+6\pm4$
2800	$+6^{+5}_{-4}$
3000	$+7^{+9}_{-7}$
3200	$+10\pm10$
3400	$+30^{+13}_{-20}$
3600	$+40\pm30$
3800	$+70^{+60}_{-40}$
4000	$+80^{+80}_{-60}$

Table 5.7: Result of the fit to vary the hypothesis made on the mass of the boson W'.

The modified frequentist approach, also called CL_s method, consists in finding two p-values corresponding to both the H_1 and H_0 hypotheses:

$$p_{s+b}(\mu) = P_{s+b}(q \geq q^{obs})$$

$$p_b(\mu) = P_b(q \leq q^{obs}),$$

and their ratio gives the confidence level of the signal:

$$CL_S = \frac{p_{s+b}(\mu)}{1 - p_b(\mu)}.$$

Upper limits are determined excluding the range of parameters of interest for which $CL_s(\mu)$ is lower than the 95% C.L..
In case of background only, the upper limit is a random variable that depends on the observed data sample and its distribution can be predicted using MC simulation.

In Figure 5.16 is reported the limit on the ratio of σ/σ_{th} given as function of W' mass; in particular, there are the observed upper limit, the expected value of the limit and the interval of excursion of 1σ and 2σ.
The observed and expected 95% C.L. upper limits exclude the mass range below 2014 GeV, with an expected exclusion of 1818 GeV.

While in the previous case, the upper limit is given on the ratio of σ/σ_{th} as a function of $M_{W'}$, model-independent limits can be set on the production cross section of W' resonances, as shown in Figure 5.17. In this case, cross sections exclusion upper limits are set in the range 2 pb to 90 fb depending on the mass.
Those limits represent the most stringent limits so far in the all-hadronic channel.

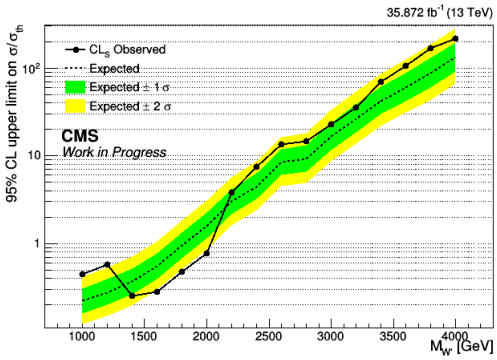

Figure 5.16: The observed and expected 95% C.L. upper limits of the W' boson ratio of the observed over expected production cross section as a function of the signal mass, assuming narrow width resonances, resulting from the fit with estimated background from data.

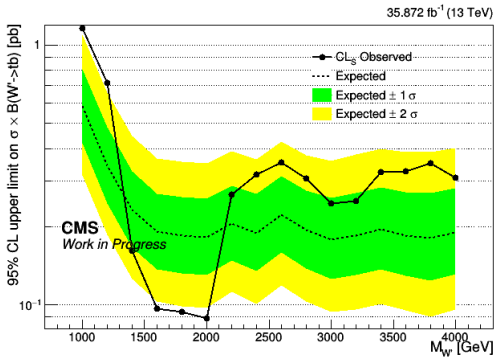

Figure 5.17: The observed and expected 95% C.L. upper limits on the W' boson production cross section as a function of the signal mass, assuming narrow width resonances, resulting from the fit with estimated background from data.

Conclusions

The aim of this thesis work is the search for a new W' resonance using 35.9 fb^{-1} of proton-proton collision data delivered by the LHC at a centre of mass energy of $\sqrt{s} = 13$ TeV, and collected by the CMS experiment in 2016.
The search is performed in the fully hadronic final states, through the intermediate decay of W' to a top quark and bottom quark pair ($W' \longrightarrow$ tb).
The Standard Model processes that contribute significantly to the background for this decay are $t\bar{t}$ pair production and QCD multijet events.
In order to discriminate the signal from the background, a series of topological and kinematic requirements are applied.
The top quark and the b quark are identified via their products of hadronization, clustered in jets of hadrons via dedicated algorithms. The mass of the W' candidate is then reconstructed from the b and top quark jets.
Since there are limits on the predictions of simulations in the region of phase space of our search, we estimate the shape and yield of background from data thanks to a Data-Driven method (DD).
A binned maximum likelihood fit in the signal region is used to test the hypothesis of the existence of a W' boson. The fit is performed on the $M_{W'}$ distribution taking into account the background estimated from data and systematic uncertainties. Different benchmark models are tested based on the hypothesis made on the W' boson mass, ranging from 1000 GeV up to 4000 GeV in steps of 200 GeV.
No significant deviation from the Standard Model expectations is observed, and therefore the results obtained with the presented analysis allow to set limits upper limits on the cross sections at 95% C.L..
This search could be improved by considering additional control samples for the systematics, to reduce even more the dependency of the data-based method on simulation assumptions, and by applying the analysis also to the data set collected by CMS in 2017 and 2018.

Bibliography

[1] CERN web, https://home.cern.

[2] LHC machine, "Journal of Instrumentation 3"no.8, (2008) S08001, https://iopscience.iop.org/article/10.1088/1748-0221/3/08/S08001.

[3] CMS web, http://cms.web.cern.ch.

[4] CMS collaboration, "The CMS tracker system project: technical design report", CERN-LHCC-98-006, http://cdsweb.cern.ch/record/368412.

[5] CMS collaboration, "The CMS tracker: addendum to the technical design report", CERN-LHCC-2000-006, http://cdsweb.cern.ch/record/490194.

[6] CMS collaboration, "The CMS electromagnetic calorimeter project: Technical Design Report", CERN-LHCC-97-033, https://cds.cern.ch/record/349375/files/ECAL_TDR.pdf.

[7] CMS collaboration, "The CMS hadron calorimeter project: Technical Design Report", CERN-LHCC-97-031, https://cds.cern.ch/record/357153/files/CMS_HCAL_TDR.pdf.

[8] The CMS collaboration, "The CMS muon project, technical design report", CERN-LHCC-97-032, https://cds.cern.ch/record/349375.

[9] CMS collaboration, "The TriDAS project, technical design report. Volume 1: The level-1 trigger", CERN-LHCC-2000-038, http://cdsweb.cern.ch/record/706847.

[10] CMS collaboration, "The TriDAS project, technical design report. Volume 2: Data acquisition and high-level trigger technical design report", CERN-LHCC-2002-026, http://cdsweb.cern.ch/record/578006.

[11] S. Glashow, "Partial-symmetries of weak interactions", Nuclear Physics, 22:579-588, (1961).

[12] S. Weinberg, "A model of leptons", Phys. Rev. Lett., 19:1264-1266, (1967).

[13] A. Salam, N. Svalthrom ed., "Elementary particle theory: relativistic groups and analyticity", Nobel symposium, (1968).

[14] F. Englert and R. Brout, "Broken Symmetry and the Mass of Gauge Vector Mesons", Phys. Rev. Lett., 13:321-323, (1964).

[15] P.W. Higgs, "Broken Symmetries and the Masses of Gauge Bosons", Phys. Rev. Lett., 13:508-509, (1964).

[16] G.S. Guralnik, C.R. Hagen and T.W.B. Kibble, "Global Conservation Laws and Massless Particles, Phys. Rev. Lett., 13: 585587, (1964).

[17] G. Zweig, "An SU(3) model for strong interaction symmetry and its breaking", Technical Report CERN-TH-401, CERN, Geneva, (1964).

[18] M.Y. Han and Y. Nambu, "Three-triplet model with double SU(3) symmetry", Phys. Rev., 139:B1006-B1010, (1965).

[19] O.W. Greenberg, "Spin and Unitary Spin Independence in a Paraquark Model of Baryons and Mesons", Phys. Rev. Lett., 13:598-602, (1964).

[20] H.D. Politzer, "Reliable perturbative results for strong interactions", Phys. Rev. Lett., 30:13461349, (1973).

[21] D.J. Gross and F. Wilczek, "Ultraviolet behavior of non-abelian gauge theories", Phys. Rev. Lett., 30:13431346, (1973).

[22] Pomarol, Alex. "117. Extra Dimensions."

[23] M. J. Dugan, H. Georgi and D. B.Kaplan, "Anatomy of a Composite Higgs Model", Nucl. Phys. B254, 299 (1985).

[24] G. F. Giudice, "Naturalness after LHC8", PoS EPS HEP2013, 163 (2013) https://arxiv.org/pdf/1307.7879.pdf.

[25] N. Arkani-Hamed, A. G. Cohen, E. Katz, A. E. Nelson, "The Littlest Higgs", JHEP 0207:034 (2002).

[26] Maiezza, Alessio, et al. "Left-right symmetry at LHC."Physical Review D 82.5 (2010): 055022.

[27] G. Altarelli, B. Mele, M. Ruiz-Altaba, "Searching for new heavy vector bosons in $p\bar{p}$ colliders.", Z. Phys. C 45, 109 (1989).

[28] Tanabashi, M. "107. W'-Boson Searches."

[29] Aaboud, M., et al. "Search for a new heavy gauge-boson resonance decaying into a lepton and missing transverse momentum in 36 fb^{-1} of pp collisions at $\sqrt{s}$= 13 TeV with the ATLAS experiment.", The European Physical Journal C 78.5 (2018): 401.

[30] Khachatryan, Vardan, et al. "Search for heavy gauge W' bosons in events with an energetic lepton and large missing transverse momentum at $\sqrt{s}$ = 13 TeV.", Physics letters B 770 (2017): 278-301.

[31] Abachi, S. "Search for right-handed W bosons and heavy W' in p $\bar{p}$ collisions at $\sqrt{s}$= 1.8 TeV."No. hep-ex/9512007. 1995.

[32] CMS collaboration. "Search for heavy resonances decaying to a top quark and a bottom quark in the lepton + jets final state in proton-proton collisions at 13 TeV.", arXiv preprint arXiv:1708.08539 (2017).

[33] CMS Collab., Phys. Rev. Lett. 117, 031802 (2016).

[34] Adair, A., et al. "Searches for W' bosons decaying to a top quark and a bottom quark in proton-proton collisions at 13 TeV."Journal of High Energy Physics 2017 (2017).

[35] CMS Collaboration, "ParticleFlow Event Reconstruction in CMS and Performance for Jets, Taus, and E T miss ", CMS Physics Analysis Summary CMS-PAS-PFT-09-001, 2009.

[36] CMS Collaboration, "Commissioning of the Particle-flow Event Reconstruction with the first LHC collisions recorded in the CMS detector", CMS Physics Analysis Summary CMS-PAS-PFT-10-001, 2010.

[37] M. Cacciari, G. P. Salam and G. Soyez, "The anti-k_T jet clustering algorithm", JHEP 04 063 (2008), https://arxiv.org/abs/0802.1189.

[38] Salam, Gavin P. "Towards jetography.", The European Physical Journal C 67.3-4 (2010): 637-686.

[39] CMS Collaboration, "Identification of b-quark jets with the CMS experiment", JINST 8 (2013) P04013, https://arxiv.org/abs/1211.4462.

[40] CMS Collaboration, "Identification of b quark jets at the CMS experiment in the LHC Run 2", CMS Physics Analysis Summary CMS-PAS-BTV-15-001, 2016.

[41] CMS Collaboration, "Top Tagging with New Approaches", CMS Physics Analysis Summary CMS-PAS-JME-15-002, 2016.

[42] Ellis, Stephen D., Christopher K. Vermilion, and Jonathan R. Walsh. "Recombination algorithms and jet substructure: pruning as a tool for heavy particle searches."Physical Review D 81.9 (2010): 094023.

[43] Y. L. Dokshitzer, G. D. Leder, S. Moretti, and B. R. Webber, "Better jet clustering algorithms", JHEP 08 (1997) 001, doi:10.1088/1126-6708/1997/08/001,arXiv:hep-ph/9707323.

[44] J. Thaler and K. Van Tilburg, "Identifying Boosted Objects with N-subjettiness", JHEP 03 (2011) 015, doi:10.1007/JHEP03(2011)015, arXiv:1011.2268.

[45] J. Thaler and K. Van Tilburg, "Maximizing Boosted Top Identification by Minimizing N-subjettiness", JHEP 02 (2012) 093, doi:10.1007/JHEP02(2012)093,arXiv:1108.2701.

[46] CompHEP Collaboration, "CompHEP 4.4: Automatic computations from Lagrangians to events", Nucl. Instrum. Meth. A 534 (2004) 250, doi:10.1016/j.nima.2004.07.096,arXiv:hep-ph/0403113.

[47] CompHEP Collaboration, "CompHEP 4.4: Automatic computations from Lagrangians to events", Nucl.Instrum.Meth. A 534 (2004) 250, doi:10.1016/j.nima.2004.07.096,arXiv:hep-ph/0403113.

[48] S. Frixione, P. Nason, and C. Oleari, "Matching NLO QCD computations with Parton Shower simulations: the POWHEG method", JHEP 11 (2007) 070, doi:10.1088/1126-6708/2007/11/070, arXiv:0709.2092.

[49] J. Alwall et al., "MadGraph 5 : Going Beyond", JHEP 06 (2011) 128, doi:10.1007/JHEP06(2011)128, arXiv:1106.0522.

[50] CMS Collaboration, "Spring15 MC Cross Sections Twiki", (2015).

[51] T. Sjöstrand et al., "An Introduction to PYTHIA 8.2", Comput. Phys. Commun. 191 (2015) 159, doi:10.1016/j.cpc.2015.01.024,arXiv:1410.3012.

[52] G. Collaboration, "Geant4a simulation toolkit", Nucl. Instrum. Meth. 506 (2003), no. 3, 250 303, doi:http://dx.doi.org/10.1016/S0168-9002(03)01368-8.

[53] CMS Collaboration, "Cms luminosity based on pixel cluster counting summer 2013 update", CMS Physics Analysis Summary CMS-PAS-LUM-13-001,https://arxiv.org/abs/1012.2466., (2013).

[54] CMS Collaboration, "Identification of b quark jets at the CMS Experiment in theLHC Run 2", CMS Physics Analysis Summary CMS-PAS-BTV-15-001, CERN,http://cds.cern.ch/record/2138504, (2015).

[55] L. Lista, "Practical Statistics for Particle Physicists",https://arxiv.org/pdf/1609.04150.pdf

[56] CMS Collaboration, "Documentation of the RooStats-based statistics tools for Higgs PAG (rev. 106)", CMS twiki page, (2013), https://twiki.cern.ch/twiki/bin/viewauth/CMS/SWGuideHiggsAnalysis CombinedLimit?rev=106.

[57] A. L. Read., "Modified Frequentist Analysis of Search Results (The CLsMethod)", CERN OPEN, 2000-205, https://cds.cern.ch/record/451614/files/open-2000-205.pdf.

[58] T. Junk, "Confidence level computation for combining searches with small statistics", Nucl. Instrum. Meth. A 434 (1999) 435, https://arxiv.org/abs/hep-ex/9902006.

[59] G. Cowan, K. Cranmer, E. Gross, and O. Vitells, "Asymptotic formulae for likelihood-based tests of new physics", Eur. Phys. J. C 71 (2011) 1554, https://arxiv.org/abs/1007.1727.